Study of REBa2Fe3O8+δ (RE = Pr, Nd, Sm) layered perovskites as cobalt-free electrodes for symmetrical solid oxide fuel cells

Milad Moazzam, Giulio Cordaro, Maxime Vallet, Vincent Boemare, Nicolas Guiblin, Guilhem Dezanneau

Study of $REBa_2Fe_3O_{8+\delta}$ (*RE* = Pr, Nd, Sm) layered perovskites as cobalt-free electrodes for symmetrical solid oxide fuel cells

Milad Moazzam[a], Giulio Cordaro[a]*, Maxime Vallet[a,b], Vincent Boëmare[a], Nicolas Guiblin[a], Guilhem Dezanneau[a]

[a]Université Paris-Saclay, CentraleSupélec, CNRS, Laboratoire SPMS, 91190, Gif-sur-Yvette, France.

[b]Université Paris-Saclay, CentraleSupélec, ENS Paris-Saclay, CNRS, Laboratoire LMPS, 91190 Gif-sur-Yvette, France

*Corresponding author: giulio.cordaro@centralesupelec.fr

Authors email: milad.moazzam@centralesupelec.fr – maxime.vallet@centralesupelec.fr – vincent.boemare@centralesupelec.fr – nicolas.guiblin@centralesupelec.fr – guilhem.dezanneau@centralesupelec.fr

Abstract

The *RE*$Ba_2Fe_3O_{8+\delta}$ (*RE* = Nd, Sm, Pr) perovskites are investigated as potential cobalt-free electrodes in symmetrical solid oxide fuel cells (SOFCs). After the preparation of samples by a soft chemistry route, we first characterized the intrinsic properties and then determined the electrochemical performance after the deposition of porous electrodes to obtain symmetrical cells. Analytical techniques such as X-ray diffraction (XRD) at room and high temperatures, transmission electron microscopy (TEM), thermogravimetric analysis (TGA), dilatometry (TEC) and 4-probe conductivity measurements were employed to characterize exhaustively structural, thermal and electrical properties of the samples. The electrochemical characterization was further investigated through electrochemical impedance spectroscopy (EIS) as well as fuel cell testing conducted on electrolyte-supported symmetrical cells. XRD showed that all samples have a cubic structure with the $Pm\bar{3}m$ space group. However, during TEM experiments, it was observed that $SmBa_2Fe_3O_{8+\delta}$ presents a quintuple nano-ordering perovskite structure. Pr-based sample shows the highest electrical conductivity (68 S cm^{-1} at 500 °C), while $NdBa_2Fe_3O_{8+\delta}$ presents the lowest area specific resistance in air (0.47 Ω cm^2 at 600 °C) revealing that the disordered perovskite structure is more efficient than the quintuple nano-ordered phase of $SmBa_2Fe_3O_{8+\delta}$ in the oxygen reduction reaction (ORR). The use of $NdBa_2Fe_3O_{8+\delta}$ as electrodes in symmetrical cells has been demonstrated between 500 °C and 600 °C.

Keywords: *Quintuple perovskite, TEM, Cobalt-free, Cathode, Anode, Symmetrical Solid Oxide Fuel Cells*

1. Introduction

The intense industrialization of the past two centuries has exponentially escalated global energy consumption and, simultaneously, our reliance on finite and environmentally detrimental fossil fuel resources. In the quest for sustainable and cleaner energy, scientists have focused on developing innovative solutions. Among these, fuel cell technology has emerged as an efficient and environmentally friendly solution that directly converts the chemical energy of fuels into electricity. In particular, Solid Oxide Fuel Cells (SOFCs) have attracted significant attention due to their remarkable efficiency, fuel flexibility, and the potential for recovering excess heat through cogeneration power plants. However, reducing production costs and extending the lifetime of SOFCs are essential for achieving widespread commercialization [1–3]. Symmetrical SOFCs have been proposed to reduce both investment and operational costs [4–6]. In particular, the possibility of reversing the polarization of the cells has been presented as a way to decompose carbon and sulfur depositions accumulated on the electrode surface in contact with the fuel, restoring initial cell performances. Additionally, limiting the number of materials for the cell components reduces thermal stresses, enhancing the lifetime of symmetrical SOFCs. However, it is crucial to identify efficient, stable, and sustainable compounds for both oxygen reduction and hydrogen evolution reactions to validate such technology options.

Perovskite-based solid oxides represent the most promising family among the investigated compounds for symmetrical electrodes. Manganites exhibit high electronic conductivity and catalytic properties but insufficient oxide-ion conductivity and structural instability in a hydrogen-rich environment [7–11]. Cobaltites, despite their excellent mixed ion-electron conductive attributes, suffer from low mechanical compatibility, instability in reducing conditions, and safety and environmental concerns [12–15]. Conversely, ferrites present slightly lower mixed ionic and electronic conductivity when compared to cobaltites and manganites [16–19], yet they exhibit notable stability even in reducing environments [20–22]. Several single perovskite materials have been previously employed as the electrodes of symmetrical SOFCs [4–6]. Double perovskite ferrites based on strontium have been demonstrated to be suitable as symmetrical electrodes [23,24]. The best performance has been reported for $Ba_{0.5}Sr_{0.5}Fe_{0.9}Mo_{0.1}O_{3-\delta}$, achieving a peak power density of 2.28 W cm^{-2} at 800 °C [25].

One potential approach to enhance ferrite mixed conductivity involves arranging the perovskite structure into ordered layers, serving as preferential channels for oxygen ion diffusion [26–30]. Ferrites with regularly alternated layers of barium and rare earth elements (*RE*) in perovskite A-sites can be arranged in double [31–33], triple [34–38], or quintuple structures [39–42]. The nano-ordering of perovskite layers remarkably modifies the conduction properties of these compounds [43], opening the doors to countless possibilities of structural engineering to improve performance. Following this idea of A-site ordering, researchers explored several YBaCuO-type compounds belonging to the 123 family [44,45] and quintuple perovskites [46–48] as electrodes for SOFCs. Promising performance as air electrodes has been achieved for the quintuple ferrites $(GdBa)_{0.8}Ca_{0.4}Co_{0.6}Fe_{1.4}O_{6-\delta}$ [47] and $Sm_{1.875}Ba_{3.125}Fe_5O_{15-\delta}$ [48], reporting polarization resistances in air at 650 °C equal to 0.16 and 0.41 Ω cm^2, respectively.

The present study aims to explore perovskite ferrites as electrode materials for symmetrical SOFCs. Specifically, the results of structural and electrochemical characterization for $PrBa_2Fe_3O_{8+\delta}$ (PBFO), $NdBa_2Fe_3O_{8+\delta}$ (NBFO), and $SmBa_2Fe_3O_{8+\delta}$ (SBFO) are presented.

2. Materials and Methods

2.1. Samples synthesis

Microwave-assisted combustion synthesis has been employed to produce powder samples. Initially, citric acid ($C_6H_8O_7$ 99.5+% Alfa Aesar) was dissolved in a 3:1 ratio with metal cations in deionized water. Then, praseodymium ($Pr(NO_3)_3{\cdot}6H_2O$ 99.99% Alfa Aesar), neodymium ($Nd(NO_3)_3{\cdot}6H_2O$ 99.9% Alfa Aesar), or samarium (III) nitrate hexahydrate ($Sm(NO_3)_3{\cdot}6H_2O$ 99.9% STREM), with iron (III) nitrate nonahydrate ($Fe(NO_3)_3{\cdot}9H_2O$ 98.0-100.0% Alfa Aesar) and barium nitrate ($Ba(NO_3)_2$ 99.5% STREM) were added to the citric acid solution. The mixture was stirred while ammonia (20.5%, AnalaR NORMAPUR) was slowly added to adjust its pH to around 6. After the solution reached a transparent state, it was placed in a microwave oven, where an irradiation step with a power of 700 W was performed for 15-20 minutes. Irradiation completely dries the solution, resulting in black ash. The powder is ground and placed in a tubular furnace at 500 °C for 15 minutes, followed by regrinding and thermal treatments at 1100 °C for 24 hours and 1200 °C for 12 hours. The second thermal treatment was necessary to obtain the pure SBFO phase and was thus performed on all the samples to allow for comparison. After the final thermal treatment, a 6-hour ball-milling step at 300 rpm was performed using 10 mm diameter zirconia

balls in ethanol. Dense pellets were obtained by pressing uniaxially the pure-phase powders mixed with polyvinyl alcohol (1 drop per gram of powder) at 4 tons for 4 minutes with a 25 mm diameter stainless steel mold, targeting a 2-3 mm thickness. A subsequent isostatic pressing treatment at 1500 bar for 5 minutes was carried out to increase the final relative density of the pellets. Green pellets were then sintered at 1300 °C for 24 hours at 100 °C h^{-1} heating and cooling rates, maintaining the temperature at 500 °C for 2 hours during the heating ramp to remove the PVA.

2.2. Characterization techniques

Powders and pellets were analyzed at room temperature using X-ray diffraction (XRD) using a Bruker D2 Phaser with Cu Kα radiation. The data were collected on an angular range of 20° to 90°. High-temperature XRD was conducted on a Rigaku Ultra X-18 diffractometer in the temperature range from 25 °C to 750 °C, with 25 °C data acquisition intervals using a Rigaku 1000 K furnace. Le Bail profile matching of XRD patterns was performed using JANA 2006 software [49] to extract the unit cell parameter for all diffractograms. Transmission electron microscope investigations were conducted in parallel (TEM) and scanning modes (STEM) utilizing a FEI Thermofisher Titan^3 G2 80-300 microscope operated at 300 kV and equipped with a Cs probe corrector, STEM detectors, an Ultrascan 1000 XP TEM camera and a SuperX detector for energy-dispersive X-ray (EDX) analyses. Dilatometry measurements were performed through a SETARAM thermo-mechanical analysis system between 30 °C and 800 °C with 1 °C min^{-1} heating ramps in air on 10 mm bar samples obtained from previously sintered pellets. Thermogravimetric analysis (TGA) in air was carried out using a SETARAM TG92 in the 25 °C - 1000 °C range at a rate of 1 °C min^{-1} during the cooling after a 2-hour stabilization time at 1000 °C. Material stability in oxidizing and reducing environments was evaluated through XRD after 12 hours of thermal treatments at 600 °C in air and 5% H_2 in Ar. Four-probe conductivity analyses were conducted with a digital lock-in amplifier (SR850, Stanford Research Systems) on dense bar samples mounted in a quartz tube to control the atmosphere. The four contacts were made using gold ink and wires (Metalor Technologies). Conductivity measurements were performed in air, Ar, and wet 5% H_2 in Ar at a flow rate of 5 L h^{-1} from 800 °C to 25 °C during cooling.

Electrochemical impedance spectroscopy (EIS) was performed on symmetrical cells made of two symmetric porous layers of electrode materials deposited on dense cerium gadolinium oxide ($Ce_{0.9}Gd_{0.1}O_{2-\delta}$, 10CGO, Treibacher AG) electrolyte pellets [50]. CGO dense pellets were prepared

using PVA as binder, isostatic pressing at 2000 bars for 5 minutes, and sintering at 1500 °C for 6 hours. Electrodes were brush painted on top of CGO substrates as slurries made of 50% wt. powders and 50% wt. paste, consisting of terpineol (Alfa Aesar), propanol (AnalaR NORMAPUR), and ethyl cellulose (Sigma-Aldrich) in a 76:20:4 massive ratio [51]. The samples were dried at 130 °C for 6 hours and calcined at 1200 °C for 2 hours. Additional NBFO symmetrical cells were produced and tested using powders calcined at 900 °C for 2 hours (T9 NBFO sample) instead of the standard thermal treatments for powders (*i.e.*, 24 h at 1100 °C followed by 12 h at 1200 °C, indicated as T12 NBFO). Gold current collectors were applied on electrodes with a thermal treatment at 800 °C for 2 hours. EIS was conducted using a ProboStat setup and a Solartron 1260 impedance spectrometer in the 0.1 Hz - 1 MHz frequency range in flowing air (5 L h^{-1}) on both sides. The measurements were collected every 25 °C, cooling the temperature from 800 °C to 500 °C, with 10 minutes of stabilization times to ensure the thermodynamic equilibrium of the samples. Complete fuel cell tests were carried out on symmetrical cells feeding separately air and wet 5% H_2 in Ar at 6 L h^{-1} flow rates in a Fiaxell testing rig using an IviumStat impedance spectrometer between 500 °C and 600 °C.

3. Results and discussion

3.1. Structural properties

3.1.1. X-ray diffraction (XRD)

The X-ray diffraction (XRD) analysis performed at room temperature on $SmBa_2Fe_3O_{8+\delta}$ powders after calcining at 1100 °C for 24 hours reveals the presence of peak splitting (Figure 1, black line). At this temperature, a pure single phase is not formed, while two cubic perovskite phases are present, probably with a different A-site composition inducing different cell parameters. One of the phases is potentially identified as $BaFeO_3$ (PDF# 14-0180), having no rare earth on the A-site of the perovskite phase. The other phase could correspond to an Sm-rich perovskite phase and be associated with the reference compound $Sr_{1-x}Sm_xFeO_{3-\delta}$ (ICSD n° 230466 [52]). The failure to produce single-phase SBFO at 1100 °C forced an additional thermal treatment at 1200 °C for 12 hours to reach phase purity. After the second calcination, the desired $SmBa_2Fe_3O_{8+\delta}$ compound is obtained (Figure 1, red line) and compared with the two reference materials $SmBa_2Fe_3O_{8.31}$ (PDF# 50-1849) or $SmBa_2Fe_3O_{7.994}$ (PDF# 50-1850). The main phase consists of the cubic $Pm\bar{3}m$ perovskite structure identified with space group n° 221. A tiny impurity peak is present at 28 °2θ

and can be attributed to the $BaFe_2O_4$ phase (PDF# 25-1191). However, the presence of this impurity phase has been considered negligible. The NBFO powder calcined at 1100 °C was formed into a dense pellet through a sintering thermal treatment at 1300 °C. The XRD result on the pellet shows that the desired SBFO phase is obtained and stable at this temperature, with only a slight cell parameter increase $\left(\frac{a_{1300}-a_{1200}}{a_{1200}} \approx 0.16\%\right)$ compared to the powders treated at 1200 °C. This

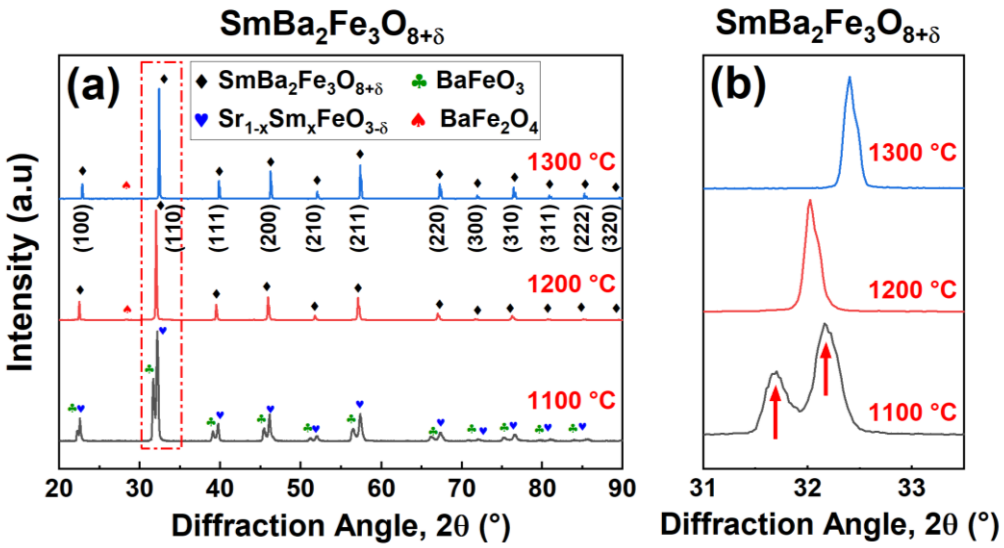

Figure 1 – Room temperature XRD diagrams of $SmBa_2Fe_3O_{8+\delta}$ powders after thermal treatment at 1100 °C for 24 h (black curve), at 1100 °C for 24 h followed by 12 h at 1200 °C (red curve), and pellet after sintering at 1300 °C (blue curve). Reflections related to reference phases are reported. Black diamonds correspond to the cubic perovskite structure indexed with the $Pm\bar{3}m$ symmetry (space group n°221, PDF# 50-1849). (b) Magnification of the highest intensity peak to highlight the splitting after the 1100 °C calcination.

cell volume expansion is possibly related to a reduction of the average Fe oxidation state due to oxygen loss above 1200 °C. Both the powders after 1100+1200 °C calcinations and the pellet after sintering at 1300 °C are considered representative of SBFO and thus employed for the following characterizations.

Figure 2 shows the diffractograms of (a) $PrBa_2Fe_3O_{8+\delta}$ and (b) $NdBa_2Fe_3O_{8+\delta}$ collected at room temperature on powders and pellet samples after each thermal treatment. Whatever the thermal treatment considered, the main phase detected is $PrBa_2Fe_3O_{8+\delta}$ and $NdBa_2Fe_3O_{8+\delta}$ (ICSD n° 50898 [36]), which can be indexed with the cubic space group $Pm\bar{3}m$ (n° 221). Conversely to SBFO, the pure single phase for PBFO and NBFO is obtained already at 1100 °C. However, the additional thermal treatment at 1200 °C is performed on all the powder materials to allow the direct

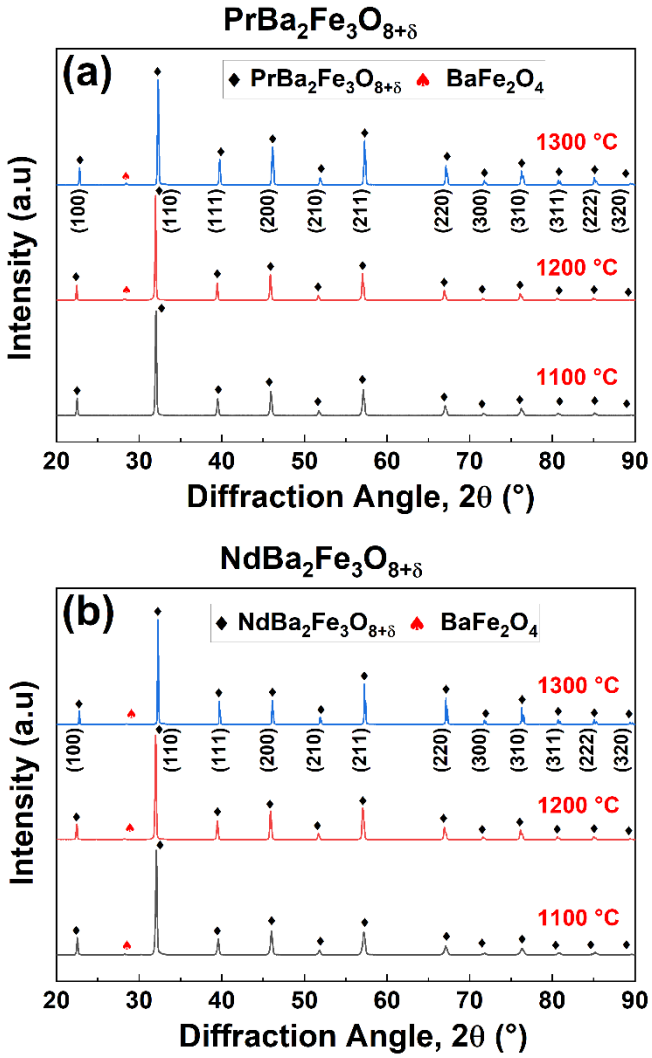

comparison with SBFO, having the same thermal history. Also for PBFO and NBFO, the tiny impurity peak at 28 °2θ, related to $BaFe_2O_4$ (PDF# 25-1191), is observed.

For all the compositions and thermal treatments, the cell parameters are deduced from a profile-matching approach and are reported in Table 1. The cell parameters for $SmBa_2Fe_3O_{8+\delta}$ and $NdBa_2Fe_3O_{8+\delta}$ are close to those reported in the literature [36]. The variation of NBFO cubic unit cell parameter after different thermal treatments is minimal, *i.e.*, below 0.01%, while PBFO lattice

Figure 2 – Room temperature XRD diagrams of $PrBa_2Fe_3O_{8+\delta}$ (a) and $NdBa_2Fe_3O_{8+\delta}$ (b) powders after thermal treatment at 1100 °C for 24 h (black curve), at 1100 °C for 24 h followed by 12 h at 1200 °C (red curve), and pellet after sintering at 1300 °C (blue curve). Reflections related to reference phases are reported. Black diamonds correspond to the cubic perovskite structure indexed with the $Pm\bar{3}m$ symmetry (space group n° 221, ICSD n° 50898) and red spades indicate the peak related to the $BaFe_2O_4$ impurity phase (PDF# 25-1191).

slightly expands after additional calcination $\left(\frac{a_{1200}-a_{1100}}{a_{1100}} \approx 0.11\%\right)$ and sintering $\left(\frac{a_{1300}-a_{1200}}{a_{1200}} \approx 0.32\%\right)$, eventually suggesting further material oxidation.

Table 1 – Comparison of the cubic lattice parameters of all samples after calcination at 1100 °C (powder), 1100 °C and 1200 °C (powder), and 1100 °C followed by sintering at 1300 °C (pellet).

	1100 °C ***a*** **(Å)**	**1200 °C** ***a*** **(Å)**	**1300 °C** ***a*** **(Å)**	**Ref. [36]** ***a*** **(Å)**
$PrBa_2Fe_3O_{8+\delta}$	3.9452±0.0001	3.9496±0.0002	3.9623±0.002	Null
$NdBa_2Fe_3O_{8+\delta}$	3.9441±0.0002	3.9474±0.0001	3.9442±0.0019	3.9598
$SmBa_2Fe_3O_{8+\delta}$	Null	3.9451±0.0001	3.9516±0.0016	3.9529

3.1.2. Transmission Electron Microscopy

Conducting a study using transmission electron microscopy (TEM) was essential to understanding the local nanostructure and chemistry of our samples. Indeed, the *RE*$Ba_2Fe_3O_{8+\delta}$ compounds were previously shown to present a long-range order different from the short-range one. Small rare earths like Sm presented more quintuple structures than those with Nd and Pr [41]. In 8-fold environments, Ba^{2+}, Pr^{3+}, Nd^{3+}, and Sm^{3+} cations have respective ionic radii of 1.42 Å, 1.126 Å, 1.109 Å, and 1.07 Å. The nano-ordering occurs when there is a significant contrast between Ba^{2+} and RE^{3+} radii, which is thus favored in the case of Sm^{3+}. However, larger REs, such as Eu and Gd, do not stabilize the quintuple structure unless tailoring the oxygen content or partially substituting Fe with Co [42]. In this work, TEM investigation was conducted on PBFO, NBFO, and SBFO powders after calcination at 1200 °C. While SBFO regularly shows quintuple nano-ordering, it was challenging to find grains with nano-ordering for NBFO, and in the case of PBFO, none was observed. Therefore, only the results of SBFO are presented in this section, while PBFO and NBFO ones are reported in the Supplementary Material.

Figure 3(a) shows the high-angle annular dark-field scanning transmission electron microscopy (HAADF-STEM) image of an SBFO thin particle with quintuple nano-ordering. Figure 3(b) is the selected area electron diffraction (SAED), representing the highlighted zone of the grain under study in the reciprocal space. The brighter dots in the (b) image correspond to the reflections of the ideal perovskite cubic structure, while the four less bright dots between every two bright dots indicate the superstructure ones. These small dots correspond to the quintuple

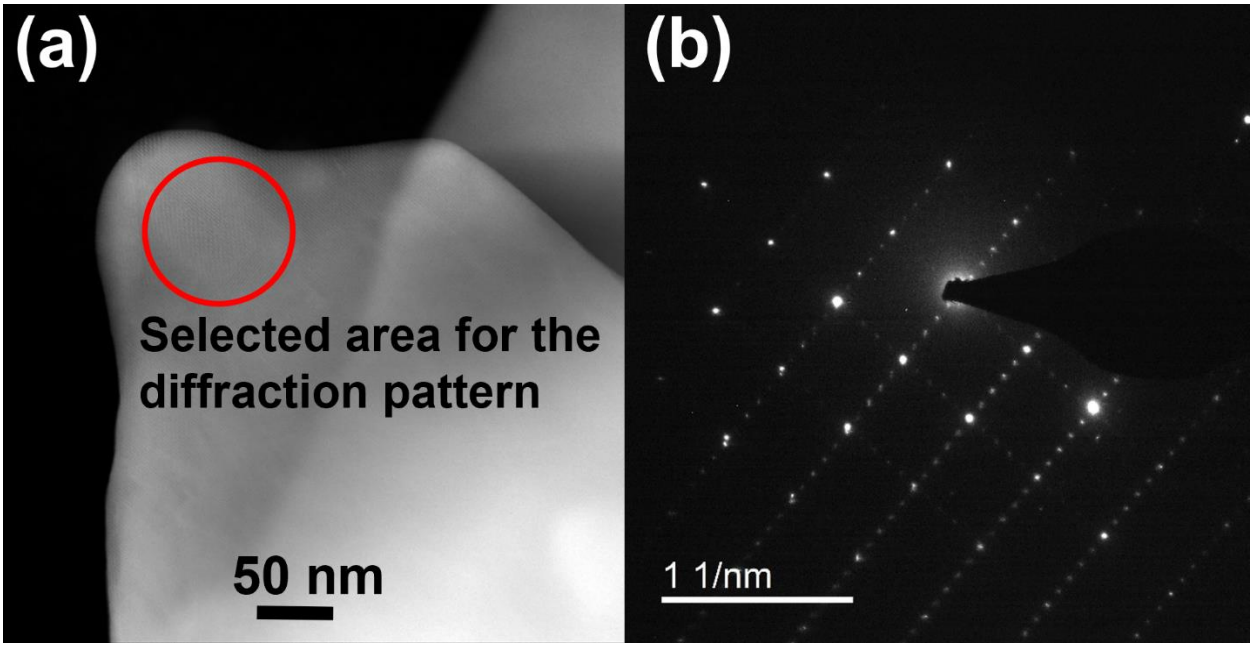

Figure 3 – High-angle annular dark-field scanning transmission electron microscopy (HAADF-STEM) image (a) and the selected area electron diffraction (SAED) image corresponding to the region highlighted of an SBFO nanoparticle with two overlapped quintuple domains oriented by 90°.

superstructure of the SBFO perovskite. They are separated by a $\frac{c^*}{5}$ distance, which coincide to a fifth of the lattice parameter of the perovskite unit cell in the direction of the superstructure in the reciprocal space. A triple layer ordering was instead expected due to the actual Ba/Sm ratio being equal to 2, under the hypothesis of an A-site plane occupied only by Sm between two layers filled only with Ba. Therefore, the presence of mixed Sm/Ba planes in the quintuple structure is necessary to respect the overall stoichiometry. For SBFO, the most correct chemical formula is thus $Sm_{1.667}Ba_{3.333}Fe_5O_{15-\delta}$.

Since quintuple dots can be observed along two perpendicular directions of the cubic structure, ordered nanodomains may switch orientation by 90° within the same matrix of cubic unit cells. This observation is further elucidated in Figure 4, where different domains are present and partially overlap inside the same particle.

Figure 4(a) shows the HAADF-STEM of an SBFO particle with domain boundaries and overlapping areas. Yellow arrows indicate in-plane domain boundaries with the same orientation of the quintuple structure. These domains present a shift of the lattice periodicity by a fraction of the superstructure periodicity (*e.g.*, less than 5 cubic unit cells) and partial overlapping (highlighted with red lines in Figure 4(c)). Additionally, a boundary with a 90° relative orientation between the

adjacent domains (blue arrow) reveals the coexistence of different orientations within the same grain. This image also shows that the quintuple perovskite nanodomains have a size of a few tens of nanometers. The small extent of the ordered domains may explain the long-range cubic structure and the absence of quintuple structure signs observed with XRD. Figure 4(b) is the fast Fourier transforms (FFT) image corresponding with the entire area shown in panel (a). As observed for SAED (Figure 3(b)), the less bright and small dots related to the quintuple nano-ordering are present in both *a*- and *b*-axis directions. Figure 4(c) summarizes the nanodomain orientations and boundaries.

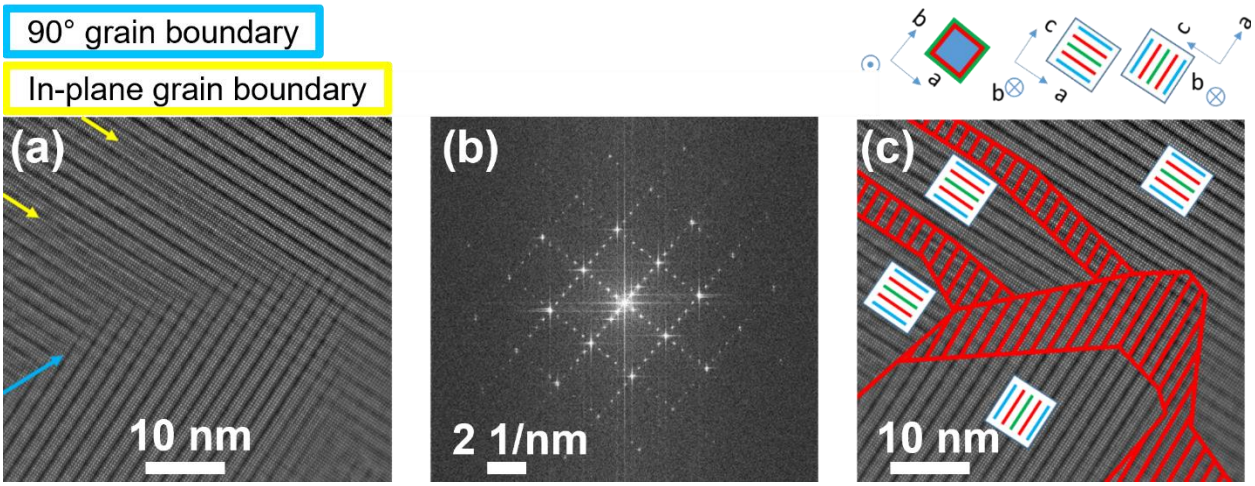

Figure 4 – HAADF-STEM image of SBFO showing different domain orientations (a), the corresponding FFT image (b), representing corresponding to the multi-domain zone (c) Domain orientation and the overlapping regions in red.

Figure 5 shows another area with different orientations. The FFT of the domains highlighted with yellow and red boxes are presented in panels (b) and (c). No superstructure ordering is observed on the left side of Figure 5(a), while on the right, the quintuple nanostructure is clearly visible. The FFT of the yellow box also confirms the existence of the quintuple nano-ordering of the domain with spots spaced by a $\frac{c^*}{5}$ vector. Another quintuple domain with the same orientation is seen in the adjacency of the yellow region, but this domain has its nano-ordering translated by a vector of 2-unit cells (along the *c*-axis) compared to the adjacent area. These two domains are separated by an anti-phase boundary highlighted by the red arrow. The domain marked with a red box indicates a regular cubic structure without any sign of quintuple nano-ordering. The corresponding FFT (Figure 5(c)) confirms this result, revealing only the big bright dots related to the cubic structure and not those of the superstructure. This result may suggest that

(i) the c-axis of the superstructure is parallel to the zone axis or (ii) the ordered and disordered structures coexist in the same SBFO crystallite.

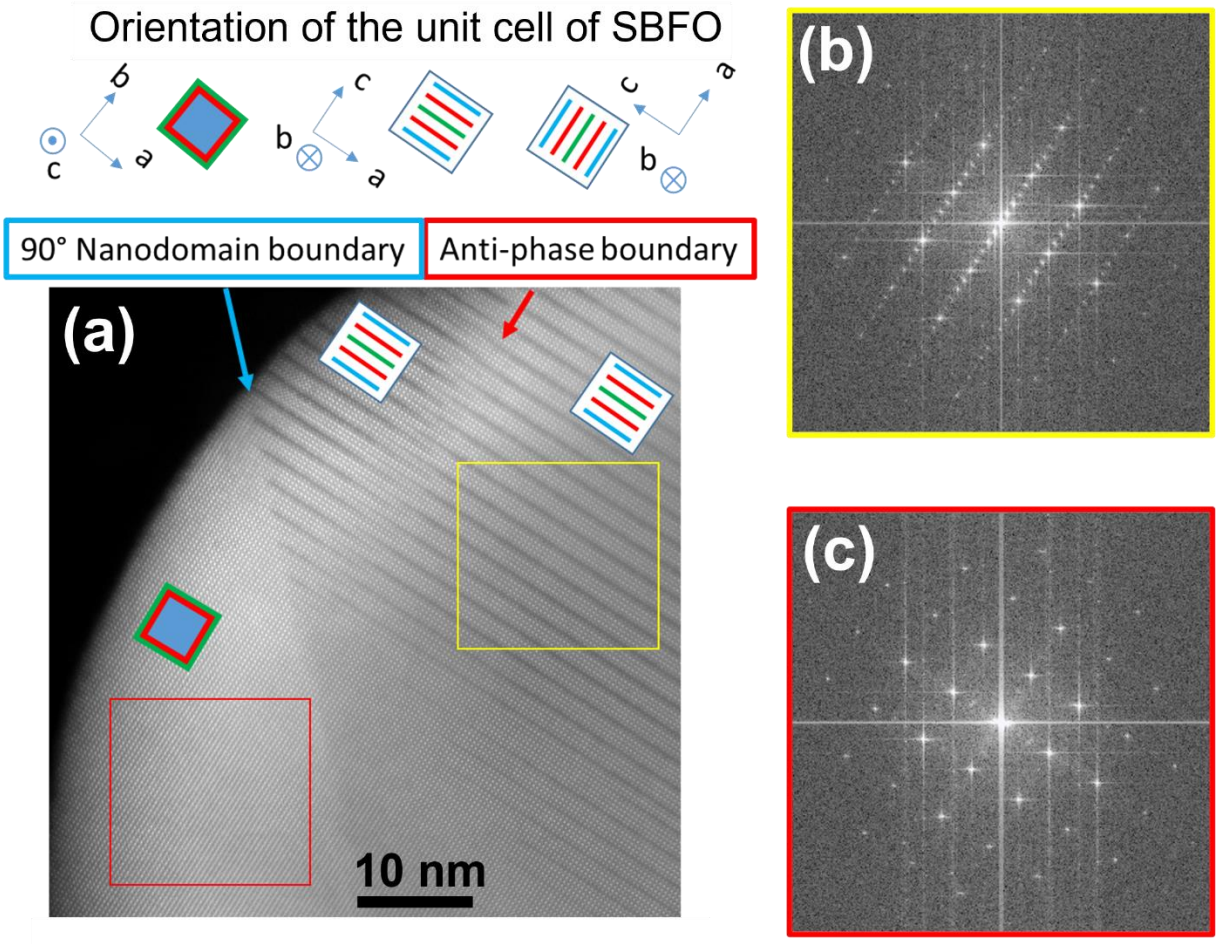

Figure 5 – HAADF-STEM image of SBFO grain edges with different nanodomain orientations and relative boundaries (a). Fast Fourier transforms (FFT) of the area inside the yellow box showing a single quintuple domain (b) and the red box representing a domain without the superstructure, possibly due to the [001] orientation or disordered cubic structure (c).

In Figure 6, the SBFO quintuple nano-ordering is studied in detail through high-resolution HAADF-STEM imaging and the associated intensity profile perpendicular to the stacking planes. In this figure, the quintuple periodicity is clearly seen, where the alternation of Sm/Ba planes and Fe planes shows a specific contrast and intensity that respects a (5**c*) periodicity, with a coherent arrangement throughout the domain. In particular, it is possible to observe planes with less intensity highlighted with red arrows. The most evident attenuation is observed for a Fe layer, followed by an A-site and other B-site planes with reduced intensity. Considering that HAADF mode mainly reveals the Z-contrast, these planes would potentially contain vacancies of a cationic

nature. Initially, it was speculated that the interplanar spaces were equal, but Figure 6(b) reveals that in the regions with the lowest intensity, the interatomic space between A-site planes increases significantly (interplanar space of region 3 = 4.42 Å, instead of 3.8 Å for region 1). This can be explained by the existence of vacancies (darker planes), which in turn would cause lower atomic attraction and more significant interplanar distance. A slight increase in the A-site interplanar distances is also observed for the two surrounding planes (marked as 2 in Figure 6(b)). This latter observation aligns with the results of Volkova *et al*. [39], who reported reduced interplanar distance between two Sm/Ba mixed planes. Their electron energy loss spectroscopy (EELS) results

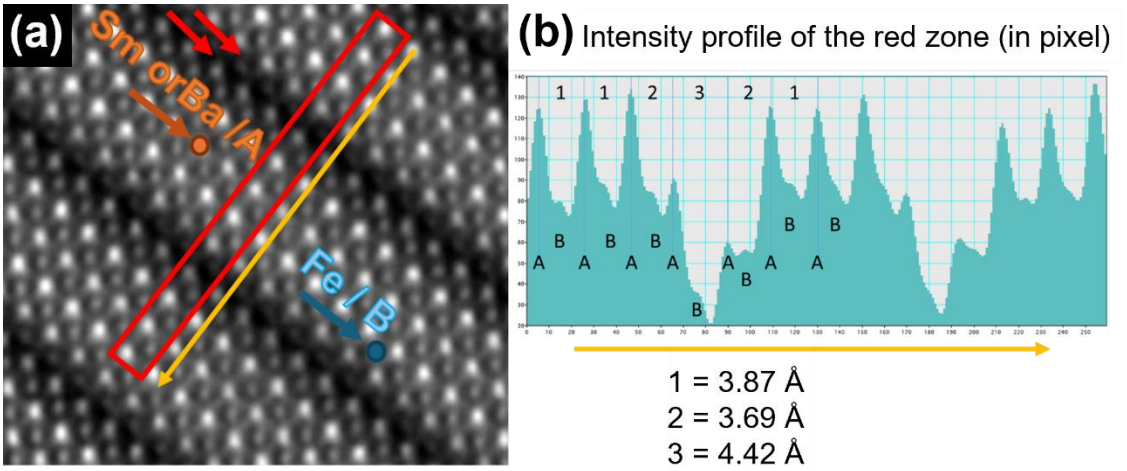

Figure 6 – High resolution HAADF-STEM image of SBFO (a) that shows the quintuple superstructure pointing out the A-site (Sm/Ba by orange arrow) and B-site (Fe by blue arrow) ordered layers. The red arrows indicate the planes where cationic deficiency is observed. (b) Intensity profile corresponding to the area selected in the red box from panel (a).

had shown a localized decrease of Fe coordination states from 6-fold to 5- or even 4-fold, correlated to oxygen vacancies localized in this plane.

Figure 7 shows the results of Energy Dispersive X-ray (EDX) spectroscopy performed on the HAADF-STEM image. Ba, Fe, Sm, and O signals are integrated to create maps and visualize the local chemistry of the quintuple structure. As can be seen in panel (c), the color overlay reveals that the quintuple nano-ordering follows the regular alternation of (Sm - Ba - Sm/Ba - Sm/Ba - Ba) planes, in accordance with the superstructure observed in previous work [39]. The columns in green with high intensity represent planes of Sm where Ba is not present, and the red columns with high intensity represent Ba with no Sm presence. The two columns in the middle represent planes where both Ba and Sm coexist. This periodicity is repeated throughout the structure to form the nano-ordered quintuple perovskite domains.

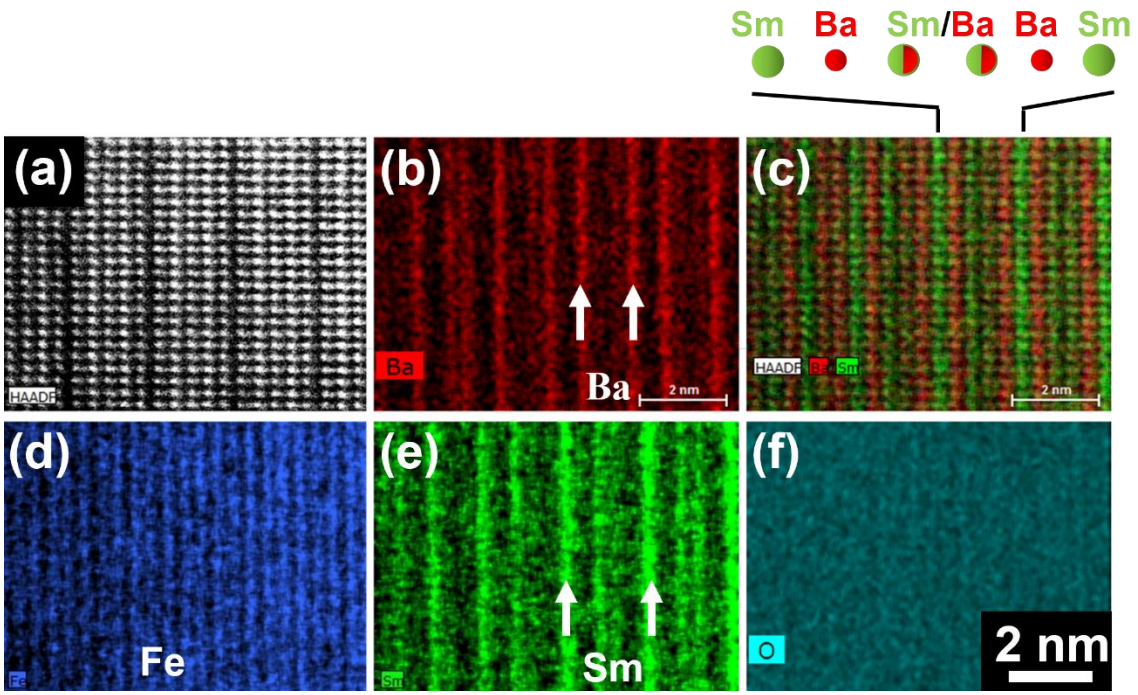

Figure 7 – Energy dispersive X-ray spectroscopy (EDX) collected on the HAADF-STEM image (a) of SBFO for Ba in red (b), Fe in blue (d), Sm in green (e), and O in cyan (f). Panel (c) present the color overlay of single atom maps.

The TEM results confirm that if stacked on each other with different orientations, quintuple nano-ordered grains can appear as cubic. This observation also explains the cubic XRD patterns seen for the SBFO samples. In order to determine the percentage of quintuple ordering and actual cubic structure in our samples, further investigation is required.

A complementary Molecular Dynamics (MD) investigation was carried out to study the quintuple superstructure influence on the oxygen ion conductivity [43]. Unfortunately, the results showed that the isotropic oxygen diffusion coefficient of the disordered structure is higher than the ordered anisotropic ones. Therefore, regarding oxygen diffusion, the quintuple nano-ordered structure of SBFO is not expected to improve the electrochemical performance compared to NBFO and PBFO.

3.2. High-temperature characterization

3.2.1. High-temperature XRD

The high-temperature XRD study was performed on all compounds to evaluate the unit cell variation in the operating temperature range of SOFCs. Figure 8 shows the XRD pattern of the NBFO sample from 100 °C to 700 °C with 100 °C intervals. As for room temperature, all diffractograms can be indexed with the cubic $Pm\bar{3}m$ symmetry and present the tiny peak at 28 °2θ related to the $BaFe_2O_4$ impurity phase. All XRD diagrams show a left-ward shift of the peaks'

location as temperature increases, reflecting the gradual growth of cell parameters due to thermal expansion. The same results are observed for PBFO and SBFO samples (Figures S1 and S2 of the Supplementary Material).

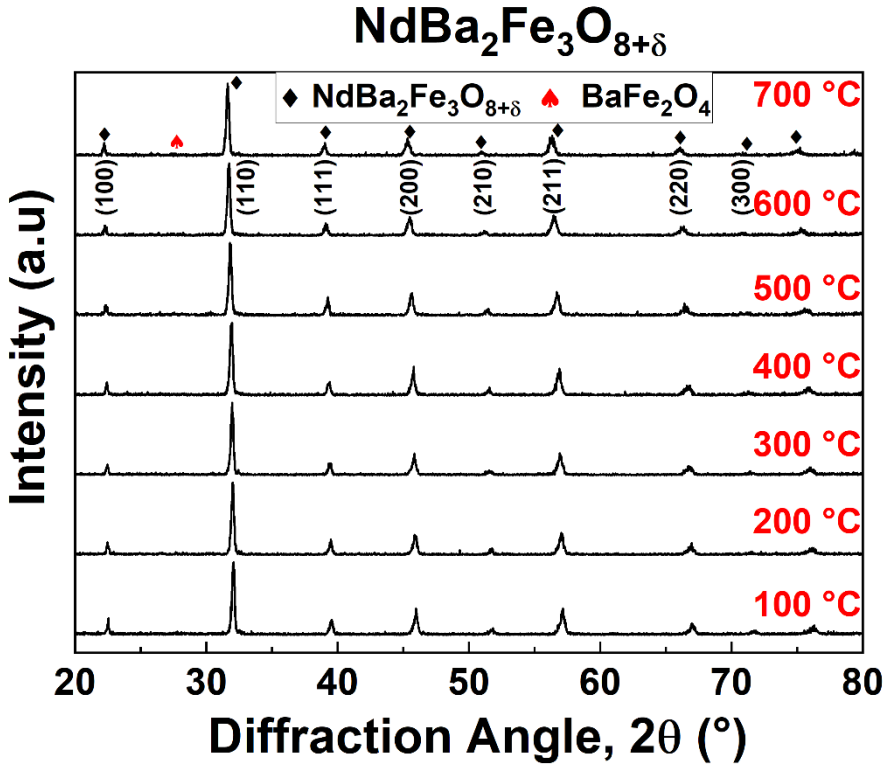

Figure 8 – High-temperature XRD diagrams of NBFO powder sample colleted between 100 °C and 700 °C in air. Reflections related to the reference $NdBa_2Fe_3O_{8+\delta}$ phase ($Pm\bar{3}m$ symmetry, space group n° 221, ICSD n° 50898) are marked as black diamonds. Red spade symbol indicates the peak related to the $BaFe_2O_4$ impurity phase (PDF# 25-1191).

The cubic unit cell parameter is calculated for each diffractogram for all the samples. Figure 9 shows the variation of lattice parameters with temperature for PBFO, NBFO, and SBFO calculated as $\left(\frac{a-a_0}{a_0}\right)$. This variation appears to be non-linear, and the temperature range has thus been divided into three different regions: low-temperature (LT), intermediate-temperature (IT), and high-temperature (HT). In the LT region, all samples experience a similar lattice parameter growth up to ~400 °C. In the HT range, the unit cell thermal expansion of PBFO and NBFO is remarkably more significant than the expansion of SBFO. This effect can be related to the different evolution of the oxygen content in these samples, as discussed in Section 3.2.3.

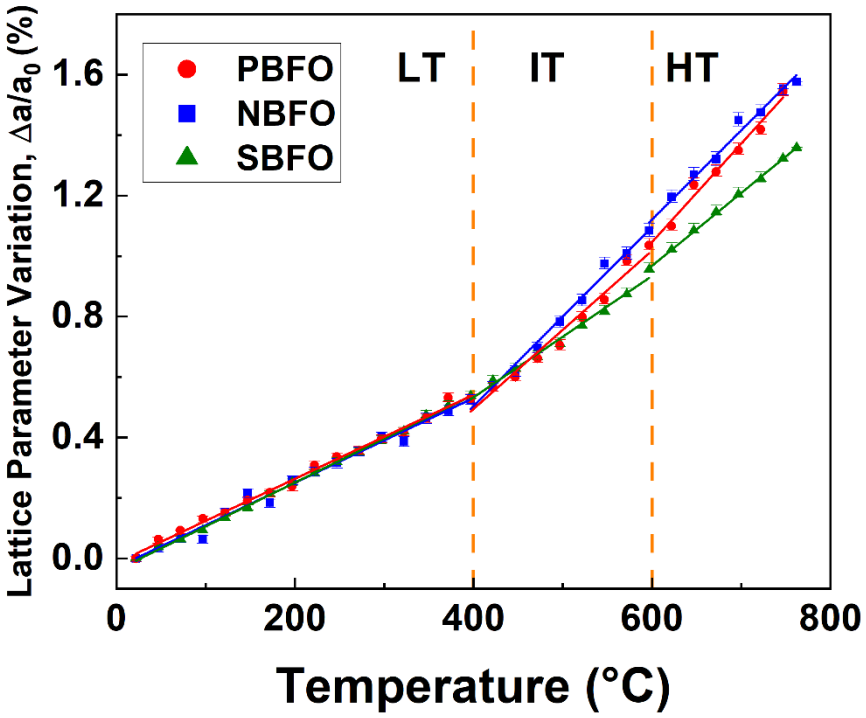

Figure 9 – Thermal evolution of PBFO, NBFO and SBFO lattice parameters obtained from HT-XRD performed from 25 °C to 750 °C every 25 °C. Three regions are highlighted: low temperature (LT), intermediate temperature (IT), and high temperature (HT).

3.2.2. Dilatometry

Figure 10 shows the thermal expansion curves for PBFO, NBFO, and SBFO measured by dilatometry over the 30-800 °C temperature range. The thermal expansion coefficient (TEC) can be obtained by extracting the slope of the $\left(\frac{L-L_0}{L_0}\right)$ curves as a function of temperature. As for the HT-XRD results, the dilatometry curves do not evolve linearly, and the temperature range has also been divided into LT, IT, and HT regions. Table 2 presents the thermal expansion coefficient of PBFO, NBFO, and SBFO using dilatometry and HT-XRD. The TECs present very similar values as measured through XRD and dilatometry. The slightly smaller value found for dilatometry could be due to the difficulty of reaching equilibrium in samples for dilatometry due to their high density, even if the cooling ramp was chosen to be slow (1 °C h^{-1}). In the LT range, all samples have a similar TEC, while above 400 °C, PBFO and NBFO present higher values than SBFO. As a whole, if thermal expansion at low temperatures is relatively close to the values of common electrolyte materials (10.5 × 10^{-6} K^{-1} for $Zr_{0.85}Y_{0.15}O_{2-\delta}$ (8YSZ), 12.5 × 10^{-6} K^{-1} for CGO [53]), in the HT range the large values (between 25-30 × 10^{-6} K^{-1}) could potentially hamper the long-term

performance of the working devices. These values are in line with TECs of other barium ferrites reported in the literature [54–56].

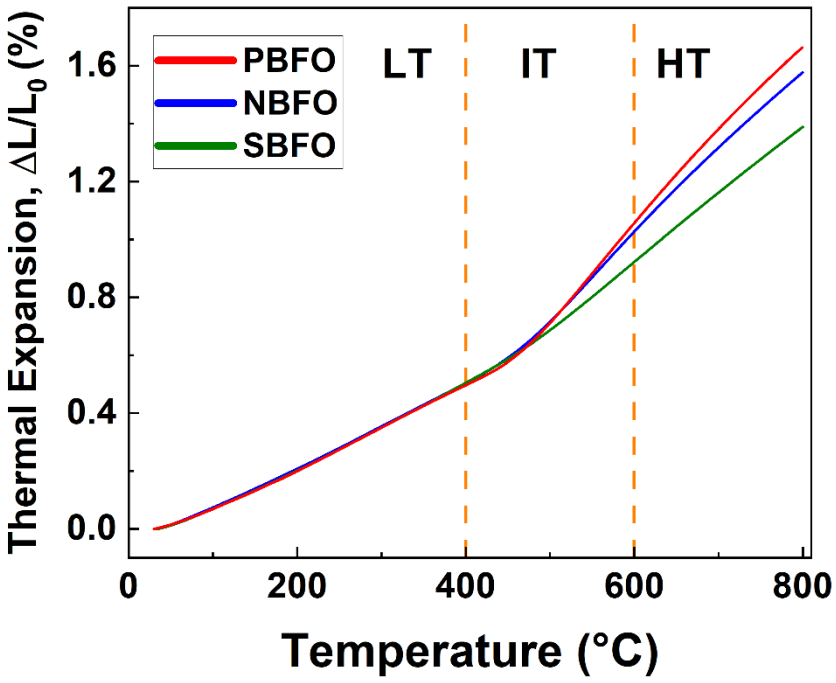

Figure 10 – Thermal expansion of NBFO, PBFO and SBFO measured by dilatometry between 30 °C and 800 °C in air.

Table 2 – Thermal expansion coefficients (TEC) values expressed in (10^{-6} K^{-1}) of PBFO, NBFO, and SBFO calculated from dilatometry and HT-XRD in the low- (LT) and high-temperature (HT) ranges.

TEC	**PBFO**		**NBFO**		**SBFO**	
(Values in 10^{-6} K^{-1})	**Dilatometry**	**HT-XRD**	**Dilatometry**	**HT-XRD**	**Dilatometry**	**HT-XRD**
LT Range (25-400 °C)	14.0	13.9	13.9	14.0	14.1	14.5
HT Range (600-800 °C)	30.5	32.6	27.5	29.5	23.4	24.1

3.2.3. Thermogravimetric analysis (TGA)

Figure 11 shows the weight loss of all samples measured by TGA cooling from 1000 °C down to 150 °C in air. A general trend of losing weight as the temperature rises is observed. Below 400 °C, all samples have a similar weight reduction, but as temperature increases, SBFO loses less mass compared to NBFO and PBFO. Below 500 °C, NBFO and PBFO show comparable weight loss rates, but as the temperature increases, PBFO presents the highest mass reduction. The weight loss as temperature increases is associated with the loss of lattice oxygen in the compounds. A change in the transition metal oxidation state accompanies the oxygen loss to maintain charge neutrality. The only species susceptible to reduction is iron, which increases the mean ionic radius (Fe^{4+} = 0.585 Å, Fe^{3+} = 0.645 Å, and Fe^{2+} = 0.780 Å for 6 coordinated high-spin cations [57]), leading to an expansion of the lattice. This explanation is coherent with the trend observed for the thermal expansion evolution (*i.e.*, $TEC_{SBFO} < TEC_{NBFO} < TEC_{PBFO}$).

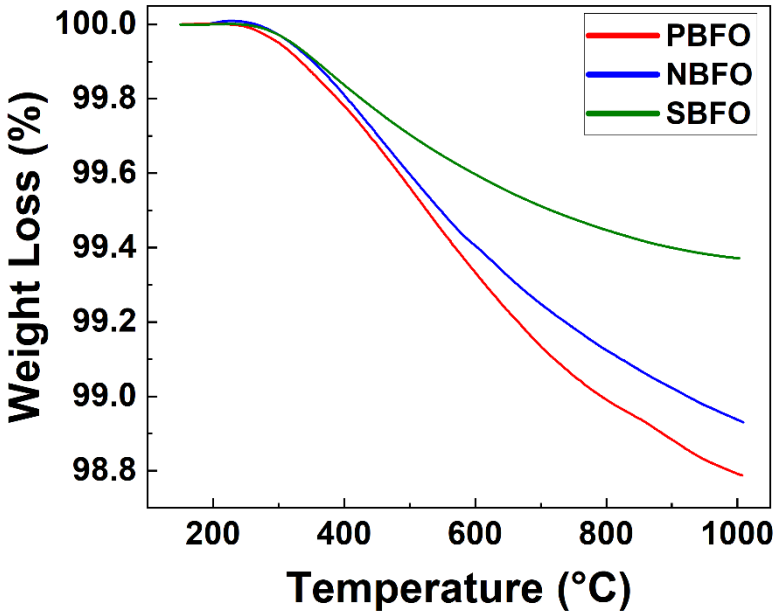

Figure 11 – Weight loss of PBFO, NBFO, and SBFO in air as a function of temperature measured by thermogravimetric analysis (TGA).

3.3. Chemical stability

Additional XRD analysis was performed after exposures to both oxidizing and reducing atmospheres at high temperatures to probe the material stability in working conditions as symmetrical SOFC electrodes. Figure 12 shows the XRD patterns for the NBFO sample after 12 hours at 600 °C in air and 5% H_2 in Ar (data for PBFO and SBFO are shown in Figures S3 and S4 of the Supplementary Material). Across all samples, no additional peaks appear; therefore, no parasitic phases are produced after thermal treatments. All the peaks remain indexed within a cubic structure with $Pm\bar{3}m$ symmetry. The impurity phase of $BaFe_2O_4$ is present in all samples. After the thermal treatment in air, the powders preserved their original black color, whereas they turned reddish-brown after the H_2-Ar test. This reddish-brown color might be associated with a mixture of Fe^{2+} (red in most oxides) and Fe^{3+} (brown in most oxides) cations. Additionally, a peak shift

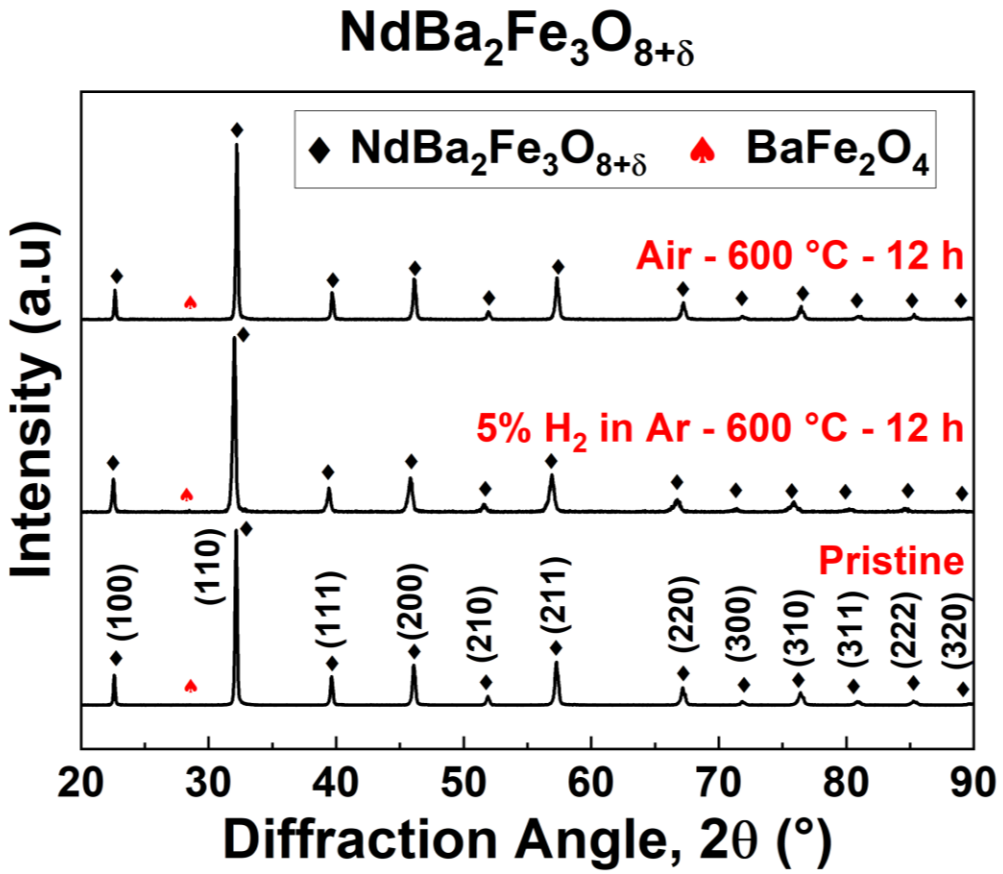

Figure 12 – XRD diagrams for NBFO after thermal treatment in oxidizing (Air) and reducing (5% H_2 in Ar) environments at 600 °C for 12 h. Reflections related to the reference $NdBa_2Fe_3O_{8+\delta}$ phase ($Pm\bar{3}m$ symmetry, space group n° 221, ICSD n° 50898) are marked as black diamonds. Red spade symbol indicates the peak related to the $BaFe_2O_4$ impurity phase (PDF# 25-1191).

towards lower angles is observed after exposure to reducing conditions, suggesting a lattice expansion and, thus, Fe reduction.

These materials are proposed as SOFC symmetrical electrodes. Therefore, the influence of the atmosphere on the B-site mixed valence is expected to impact the electrochemical properties of the anode and cathode sides differently. Nevertheless, the stability of the structure indicates that these compounds can be applied as electrode materials for both oxidizing and reducing atmospheres.

3.4. Electrical properties

The conductivity measurements in oxidizing and reducing conditions are necessary to understand the conduction mechanisms of the samples and their suitability as symmetrical SOFC electrodes. Figure 13 shows the total conductivity of PBFO, NBFO, and SBFO measured in air, Ar, and wet 5% H_2 in Ar ($p_{H2O} \approx 0.023$ bar). PBFO has a slightly higher conductivity in air than NBFO, whereas the SBFO sample has a considerably lower conductivity. The maximum conductivities in air were recorded between 300 and 400 °C and are equal to 68, 43, and 9 S cm^{-1} for PBFO, NBFO, and SBFO, respectively. The results for SBFO are in line with the literature [48].

The fact that the conductivity increases at low temperatures and reduces above 400 °C means that both the concentration and mobility of charge carriers are affected by temperature changes in a given atmosphere. In this type of compound, the electrical behavior is mainly of polaronic nature, where electrons jump from one Fe site to another, with ions' dynamics assisting the hopping [48,58,59]. The mobility in such cases usually follows an Arrhenius law with a given activation energy. Since conductivity is not increasing exponentially with temperature, the number of charge carriers also evolves. This result can be connected with the oxygen loss reported previously. If we consider the formula $NdBa_2Fe_3O_{8.5}$, with an oxygen content at room temperature measured by iodometry [35–37], the oxidation state of iron is thus 3.33. As temperature increases, oxygen loss leads to a reduction of the mean iron oxidation state and, therefore, to a potential drop in charge carrier concentration. As measured by TGA (Figure 11), below 400 °C, the oxygen loss is insignificant, and the conductivity increase is driven by a charge mobility enhancement. At high temperatures, the rise in charge mobility is compensated by reducing charge carriers due to oxygen

loss. Therefore, the conductivity behavior stabilizes (SBFO) or even starts to decrease (PBFO and NBFO) above 400 °C.

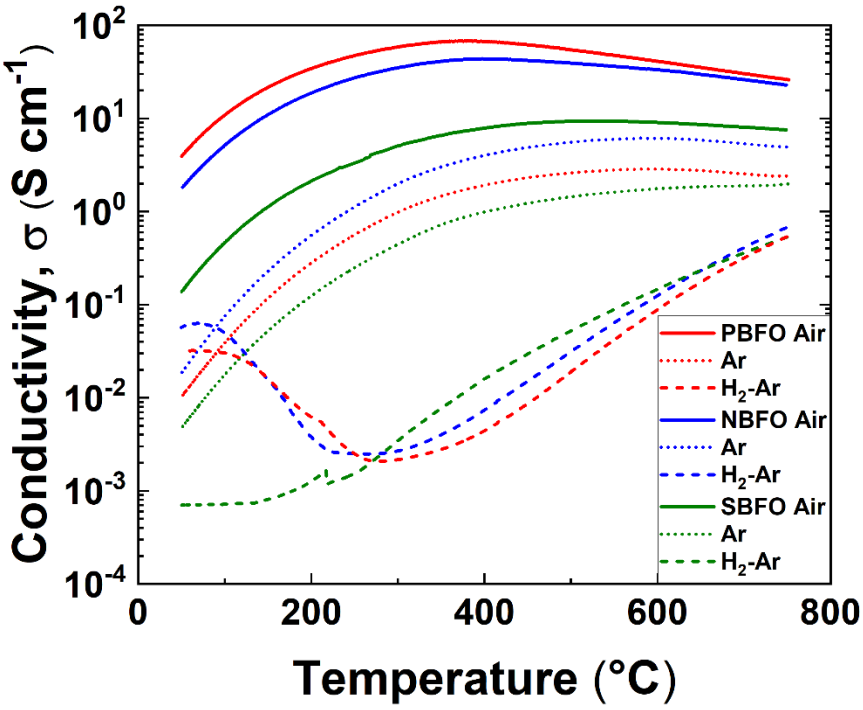

Figure 13 – Total conductivity of PBFO, NBFO, and SBFO measured between 50 and 750 °C in air, Ar, and 5% H_2 in Ar.

The conductivity results in Ar present a different trend than air among the compounds. The most conductive material in Ar is NBFO, followed by PBFO, while the lowest values are again observed for SBFO, as for air results. Still, the gap between the 3 compounds is reduced in Ar compared to air. Generally, the Ar conductivity is one order of magnitude lower than air, which can be explained by reduced average oxygen contents and, thus, decreased charge carrier concentrations. The compensation behavior between charge carrier concentration and mobility can also be observed.

In 5% H_2 in Ar, the conductivity decreases by several orders of magnitude compared to air. As mentioned above, Fe reduction is believed to be detrimental to electrical conductivity due to the decrease of charge carriers. The curves do not present the maximum between 300-400 °C but increase monotonically with temperature. Below 250 °C, NBFO and PBFO show an unexpected rise in conductivity. This phenomenon has not been fully understood, but it is outside the operative range of SOFCs.

From these results, the conductivity of NBFO and PBFO in air between 500 and 750 °C ranges from 23 to 55 S cm^{-1}. These values are lower than the target value of 100 S cm^{-1}, proposed by Steele [60], to ensure the absence of conduction limitations in the cathodic polarization resistance. For an air electrode, this limitation increases the ohmic resistance of impedance results due to the lack of electrons at the oxygen reduction reaction sites. However, conductivities between 10 and 100 S cm^{-1} are potentially sufficient for electron transport in mixed electronic and ionic conductors (MIEC). Particular attention was paid to ohmic resistances during EIS analysis, and more details are presented in Section 3.5.2. Conversely, the conductivity values in the H_2/Ar mixture suggest that limitations might arise at the fuel side of the symmetrical SOFC. We nevertheless keep in mind that real devices would work on pure hydrogen, for which this family of ferrites is expected to present *n*-type conductivity at very low pO_2 conditions [61]. On the other hand, the increase of conductivity at high oxygen levels also confirms the existence of *p*-type contribution.

3.5. Electrochemical performance

3.5.1. Electrochemical characterization of PBFO, NBFO and SBFO electrodes

The electrochemical performance of PBFO, NBFO, and SBFO electrodes was evaluated in the symmetrical cell configuration through electrochemical impedance spectroscopy (EIS). Electrode layers' mechanical stability and adhesion on electrolyte supports are essential for reliable EIS results. Low mechanical resistance of the electrode can cause significant degradation during EIS measurements due to partial detachment and subsequent active area reduction. Poor adhesion can hamper the charge transfer processes at the electrode/electrolyte interface, adding resistive contributions unrelated to the intrinsic electrode properties. The extreme case is delamination, which also contributes to additional ohmic resistance. These crucial factors were considered when optimizing the symmetrical cell production by tailoring powder size and microstructure, slurry preparation and deposition, electrolyte selection, and thermal treatments. The results of the parameters optimization are not presented in detail in this study, but a systematic EIS study was performed. The resistance was minimized by varying the electrolyte support material among LSGM ($La_{0.8}Sr_{0.2}Ga_{0.8}Mg_{0.2}O_{3-\delta}$), CSO ($Ce_{0.9}Sm_{0.1}O_{2-\delta}$), and CGO ($Ce_{0.9}Gd_{0.1}O_{2-\delta}$). The latter was selected due to excellent adhesion and lack of reactivity between electrodes and electrolyte powders. The reactivity between electrodes and electrolytes was verified by XRD on *post-mortem* cells of NBFO (not shown). Meanwhile, the temperature for calcining the ink deposited on the

electrolyte to prepare the porous layers was optimized inside the 950-1250 °C range. Finally, the electrode thickness was evaluated between 5 and 30 µm. The best performance was obtained for symmetrical porous layers with 15 µm of thickness deposited on CGO after thermal treatment of 1200 °C for 2 hours. These optimal parameters were employed to produce PBFO, NBFO, and SBFO symmetrical cells for EIS measurements.

Figure 14 shows the impedance spectra in Nyquist plots collected at 550-800 °C in air inside the 0.1-10^6 Hz frequency range. Significant differences in the ohmic resistance (*i.e.*, the value of the first intercept with the Z' axis) are observed due to variations in the thickness of electrolyte pellets. Therefore, this contribution is subtracted to simplify the visualization and comparison of the results. A systematic verification of the ohmic resistance values is performed by calculating the relative ionic conductivity of CGO pellets $\left(\sigma_{CGO} = \frac{thickness}{R_{Ohm} \cdot Area}\right)$ and comparing to the theoretical values. No significant reductions in CGO ionic conductivity were recorded for all the EIS results presented in this work. Additionally, the relative density of CGO pellets was measured by dividing the experimental density by the theoretical one (7.21 g cm^{-3} [62]). Only pellets with relative densities higher than 95% were employed as support for EIS.

The experimental impedance data are normalized over half of the electrode surface to obtain the area specific resistance (ASR) and subsequently fitted to measure the polarization resistance accurately by the equivalent circuit method (ECM). The equivalent circuit contains an inductance (L) in series with a resistance accounting for the ohmic contribution (R_{Ohm}) and different resistances in parallel to constant phase elements (R_{Pol}//CPE), each representing a resistive contribution involved in the electrode reaction. Fitting the EIS spectra for all samples required three R_{Pol}//CPE contributions. Excellent agreement between raw data and fitted curves is obtained (Figure 14), and the three R_{Pol} values are extracted and summed together to calculate the electrodes' ASR.

The resistance to the oxygen reduction reaction (ORR) is composed of a high-frequency (left side of the Nyquist plot), a middle-frequency, and a predominant low-frequency phenomenon (right side) for these compounds. An evident distinction between these two contributions is observed for SBFO, which also presents the most significant values, and for NBFO at temperatures lower than 700 °C. These spectra shapes indicate that further optimization of the electrodes can be performed

to reduce the global resistance [63,64]. However, NBFO shows the lowest ASR values of the series, followed by PBFO.

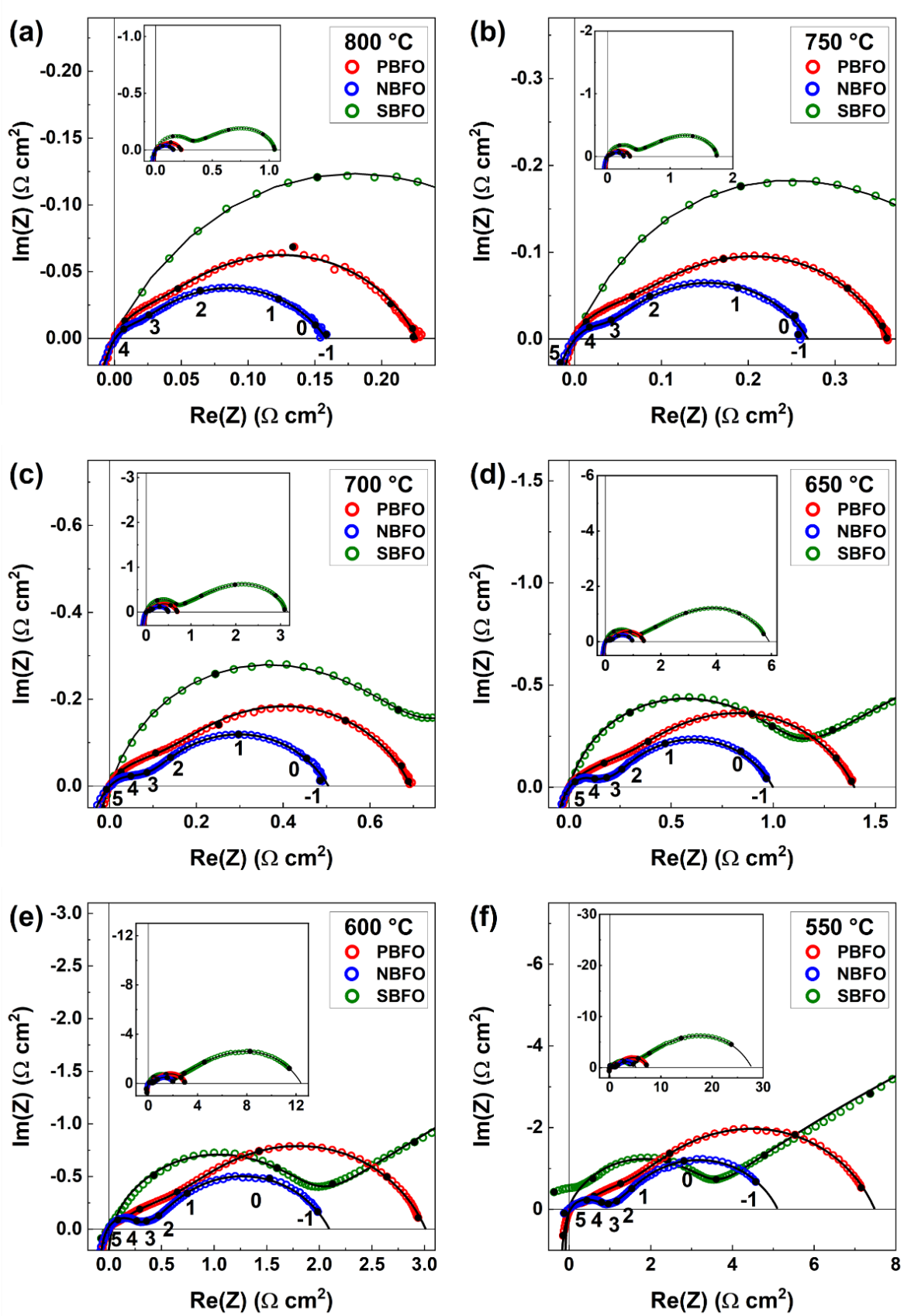

Figure 14 – Nyquist plots reporting impedance spectra of PBFO (red circles), NBFO (blue), and SBFO (green) symmetrical cells measured by EIS in air in the 0.1-10^6 Hz frequency range at 800 °C (a), 750 °C (b), 700 °C (c), 650 °C (d), 600 °C (e), and 550 °C (f). Full circles indicate the frequency decades with numbers expressing the decimal logarithm of the frequency. Black solid lines represent the fittings performed by the equivalent circuit method (ECM) using a circuit with an induction in series with a resistance and with three R//CPE contributions (resistance in parallel with constant phase element).

The ASR values of PBFO, SBFO, and NBFO are reported in the Arrhenius plot (*i.e.*, the logarithm of the resistance versus the inverse of the temperature, Figure 15). All samples present linear trends and similar activation energy around 1 eV. PBFO and NBFO results are comparable, while SBFO presents polarization resistances of almost one order of magnitude higher. The ASRs for PBFO, NBFO, and SBFO are 0.26, 0.17, and 1.29 Ω cm^2 in air at 800 °C. The much larger ASR observed for SBFO may be related to the low total conductivity observed (5.3 and 9.3 S cm^{-1} at 800 and 500 °C, respectively; Figure 13). The sluggish transfer of electrons to the reaction sites may limit the ORR and partially explain the high ASR values. However, SBFO spectra do not reveal the presence of supplementary resistive contributions compared to PBFO and NBFO. The limiting resistive phenomena are probably similar among the three materials because both the EIS spectra shapes and the ASR activation energy are comparable. Therefore, another possible explanation is related to the reduced oxygen diffusion coefficient of the nano-ordered structure, which we

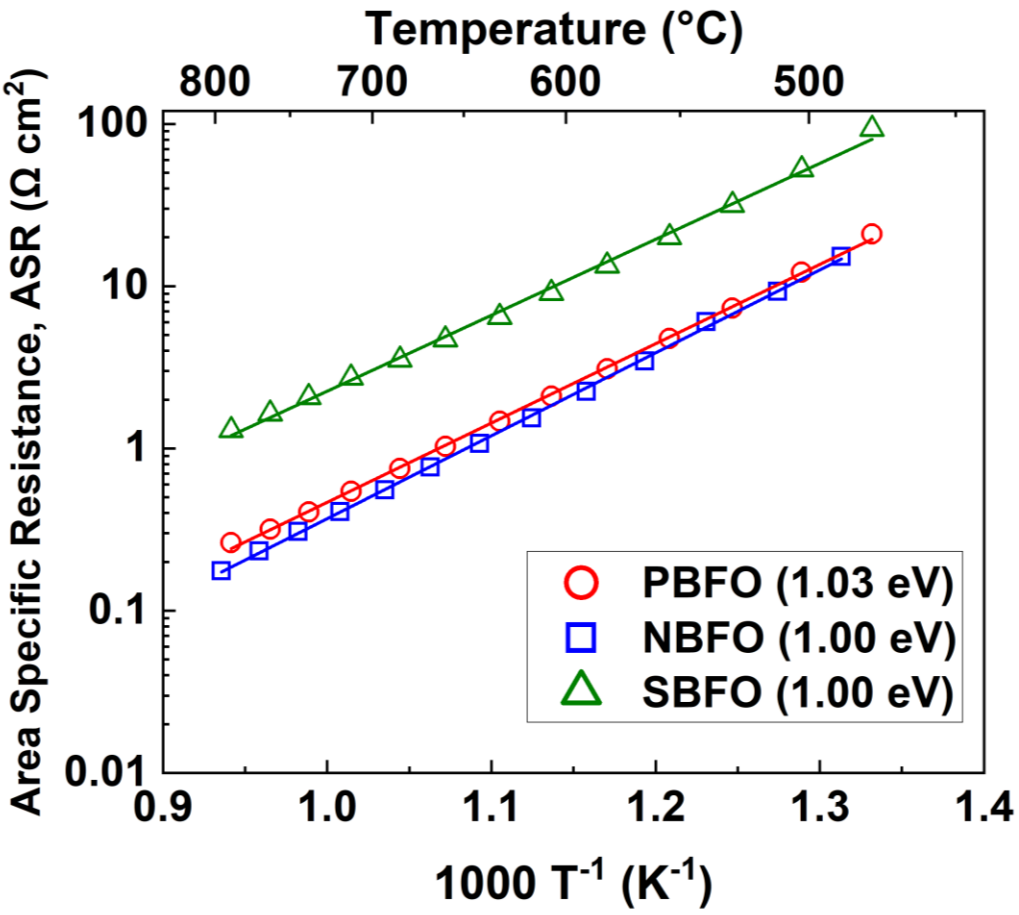

Figure 15 – Arrhenius plot of the area specific resistance (ASR) values of PBFO, NBFO, and SBFO calculated from the EIS results measured in air between 450-800 °C.

observe only for SBFO, compared to the disordered structure, *i.e.*, PBFO and NBFO [43]. Literature results on the nano-ordered quintuple perovskite $Sm_{1.875}Ba_{3.125}Fe_5O_{15-\delta}$ showed ASR values equal to 0.075 Ω cm^2 in air at 800 °C [48]. This improved result can be explained by the different stoichiometric ratios of cations and the cell fabrication parameters, *i.e.*, LSGM as electrolyte material and 1000 °C as temperature to calcine the electrode layers. Given these results, we selected NBFO composition and improved the preparation procedure to reduce the ASR values, with the aim of testing the material in fuel cell conditions.

3.5.2. Microstructural improvement of NBFO electrodes

Powders calcined at 1200 °C tend to form large agglomerates despite repeated ball-milling steps throughout the synthesis process. Reducing the grain size distribution of electrode powders increases the specific surface area and, thus, active reaction sites for the ORR. A new procedure was developed to limit the grain growth during the synthesis of NBFO powder. Instead of calcining the precursors for 24 h at 1100 °C, followed by 12 h at 1200 °C, NBFO precursors were merely treated for 2 h at 900 °C. NBFO powder calcined at 900 °C was subsequently used to produce symmetrical porous layers for EIS measurements following the exact same procedure of NBFO treated at 1200 °C. Therefore, the phase purity of NBFO was not completely obtained during the powder preparation but during the symmetrical cell production (*i.e.*, calcination of NBFO ink at 1200 °C for 2 h to obtain symmetrical porous layers on the CGO electrolyte support).

In the following sections, the NBFO electrodes produced from powder treated at 900 °C are named "T9 NBFO" to differentiate between the powders that undergo the final calcination at 1200 °C referred to as "T12 NBFO". T12 NBFO powders are the samples used for the characterizations presented in the previous sections to evaluate the properties of pure-phase NBFO composition.

The difference in microstructure between T12 and T9 NBFO electrode layers was investigated through Scanning Electron Microscopy (SEM), observing the cross sections of symmetrical cells before EIS (Figure 16). T12 NBFO electrode has average grains of 1.18 ± 0.14 µm diameter and presents large agglomerates due to powder sintering. The microstructure of the T9 NBFO layer is more uniform, without large agglomerates, and maintains good adherence with the dense CGO pellet substrate. The T9 NBFO average grain size is equal to 0.58 ± 0.11 µm, which is half of the

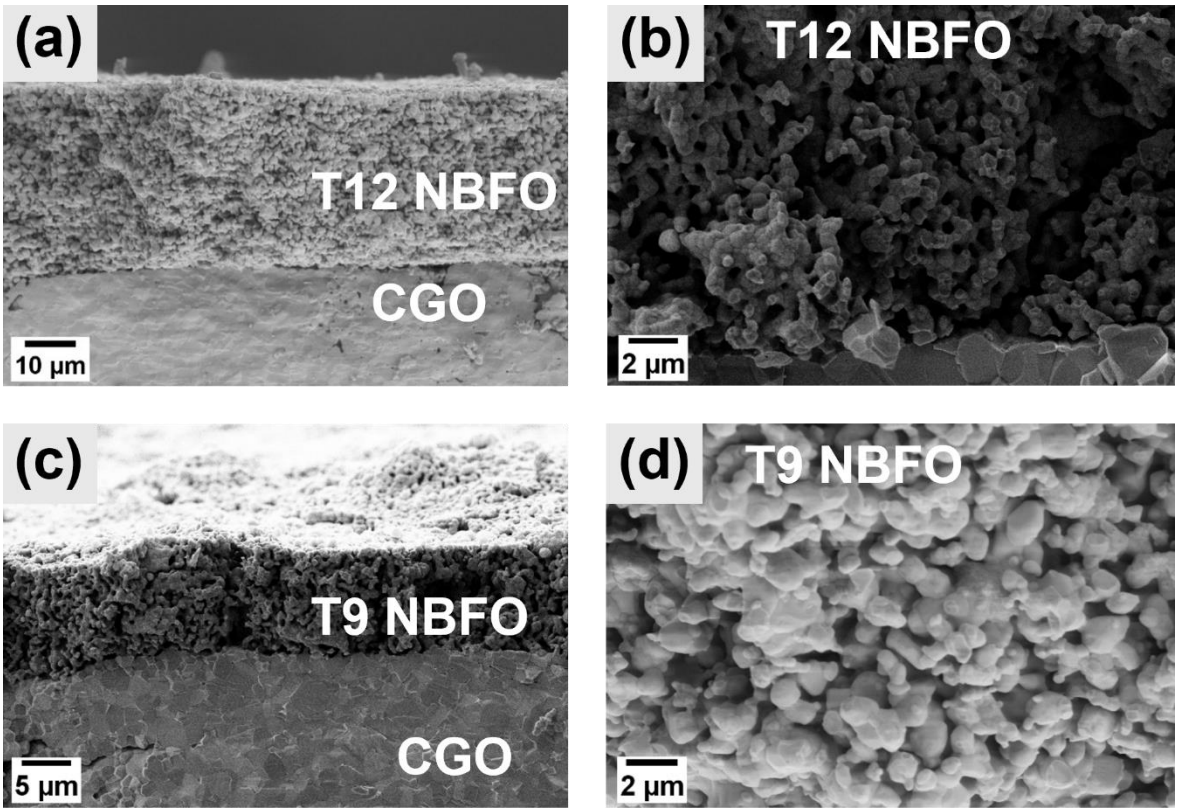

Figure 16 – SEM images of cross sections of symmetrical cells showing the microstructure of porous layers made of NBFO powders treated at 1200 °C (T12 NBFO, (a) and (b)) and at 900 °C (T9 NBFO, (c) and (d)) deposited on dense support pellet of CGO electrolyte material.

T12 NBFO electrode. Sub-micrometer particle size distribution is generally targeted as the optimal dimension for cathode powders [64–67].

The impedance spectra of T12 and T9 NBFO symmetrical cells measured in air between 550-800 °C are presented in Figure 17. The EIS results reveal that T9 NBFO exhibits significantly lower resistance values than T12 NBFO. The ASR of T9 NBFO is 0.05 Ω cm^2 at 800 °C, about a third of the ASR of T12 NBFO. The performance enhancement is attributed to the improved microstructure obtained by decreasing the NBFO powder synthesis temperature. Middle- and low-frequency contributions mainly contribute to the ASR reduction at high temperatures, where only two R//CPE contributions are necessary for the ECM fitting. The low-frequency contribution of T9 NBFO at 800 °C is probably due to gas diffusion limitation. By reducing the temperature, the spectra shape changes and becomes similar to T12 NBFO ones. Below 675 °C, using the same circuit with three R//CPE contributions is necessary to fit the spectra of both samples.

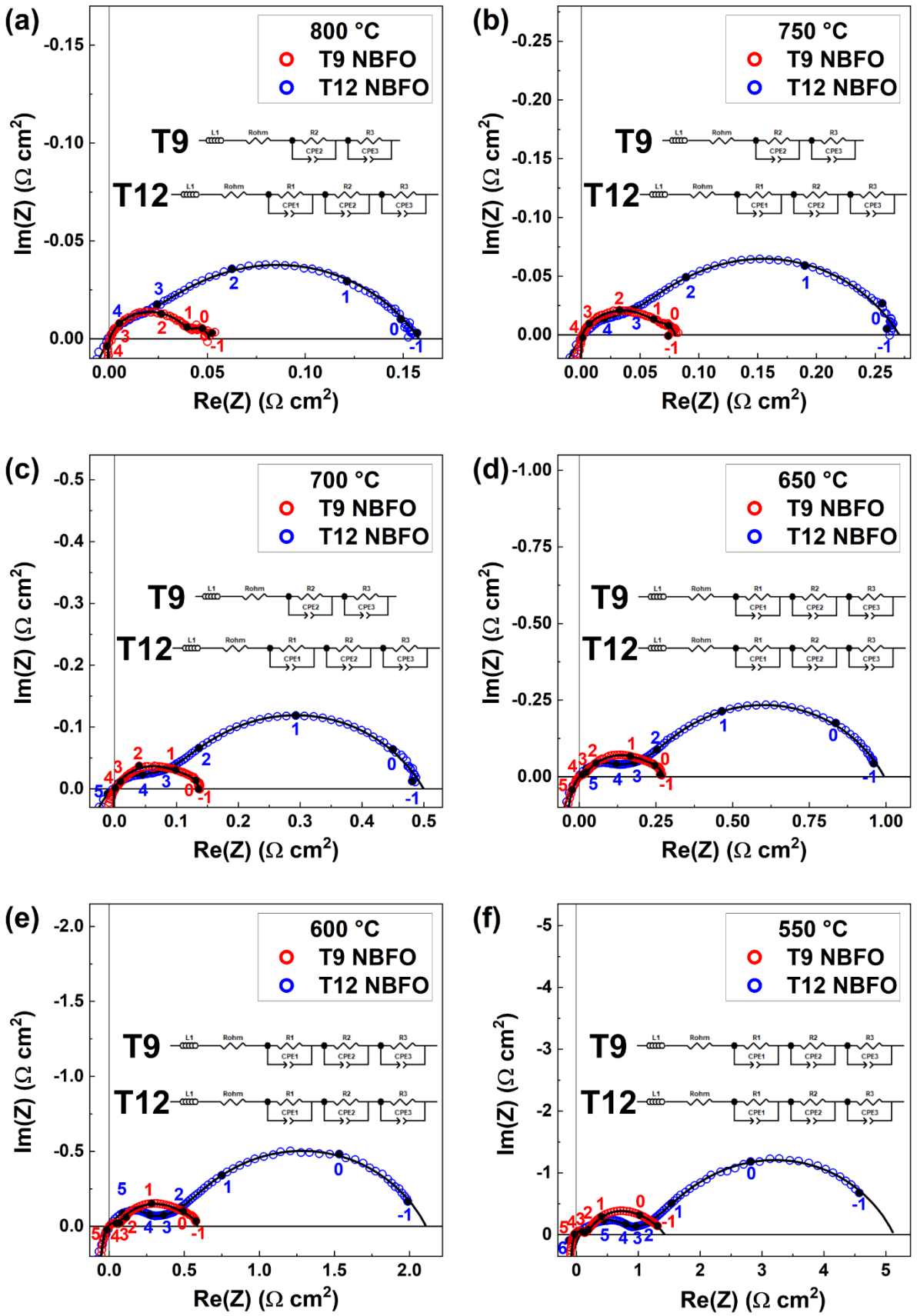

Figure 17 – Nyquist plots reporting impedance spectra of T12 (blue circles) and T9 NBFO (red) symmetrical cells measured by EIS in air in the 0.1-10^6 Hz frequency range at 800 °C (a), 750 °C (b), 700 °C (c), 650 °C (d), 600 °C (e), and 550 °C (f). Full circles indicate the frequency decades with numbers expressing the decimal logarithm of the frequency. Black solid lines represent the fittings performed by the ECM using the circuit reported in the graph. Three R//CPE contributions are employed for fitting the spectra of T12 NBFO and T9 NBFO below 650 °C, while two R//CPEs are necessary for fitting T9 NBFO at 700, 750, and 800 °C.

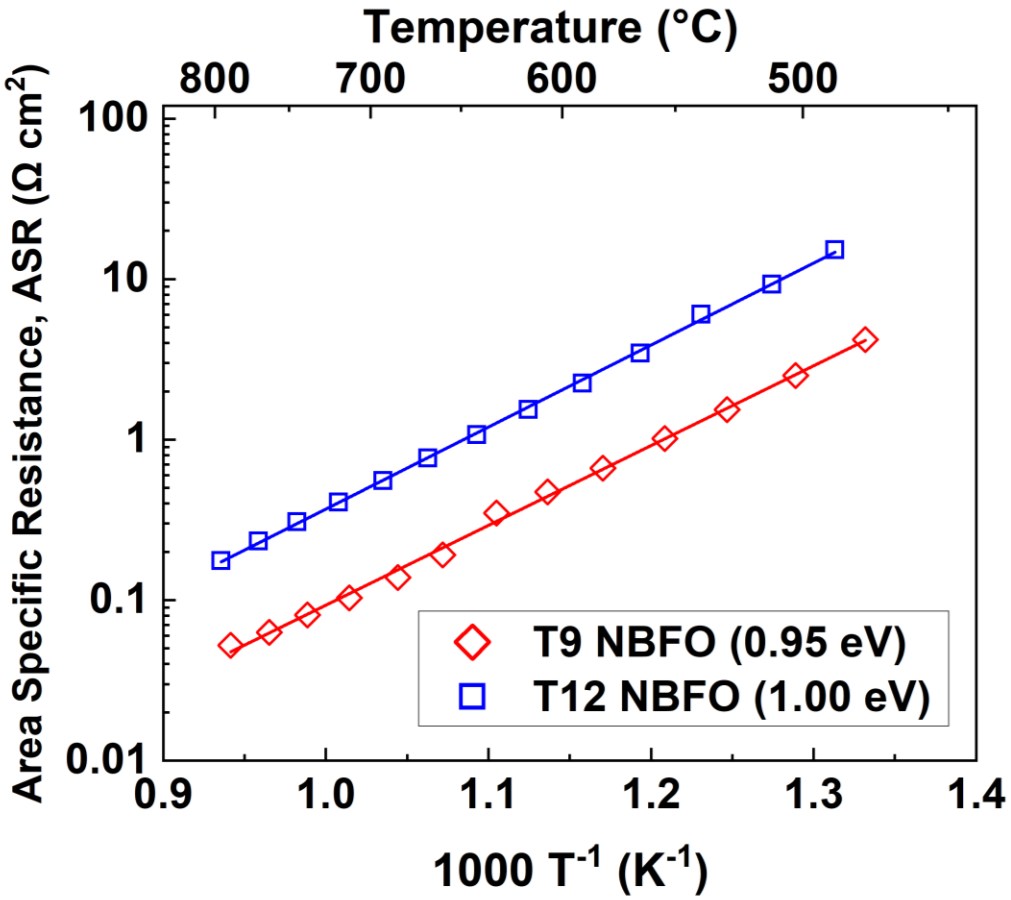

Figure 18 – Arrhenius plot of the ASR values of T12 and T9 NBFO calculated from the EIS results measured in air between 450-800 °C.

The Arrhenius plot reports the ASR values of T12 and T9 NBFO, showing linear behaviors and similar activation energies (Figure 18). Down to 650 °C, T9 NBFO presents ASR values below the 0.15 Ω cm^2 threshold proposed by Steele to be considered an efficient and promising electrode for SOFCs [68]. Therefore, these production conditions are selected for the measurements in fuel cell conditions.

3.5.3. Fuel cell measurements of T9 NBFO symmetrical cells

As an indicator of the performance of NBFO in fuel cell conditions, we collected I/V polarization curves on single cells with a symmetrical configuration of T9 NBFO/CGO/T9 NBFO. The cells were synthesized using the optimized conditions reported in Sections 3.5.1 and 3.5.2. The thickness of the CGO electrolyte support was reduced to 660 µm to minimize the ohmic resistance.

Figure 19(a) shows the cell I/V curves, and panel (b) depicts the maximum power densities as a function of temperature. At all temperatures, the OCV is in the range of 0.9 - 0.95 V. These values

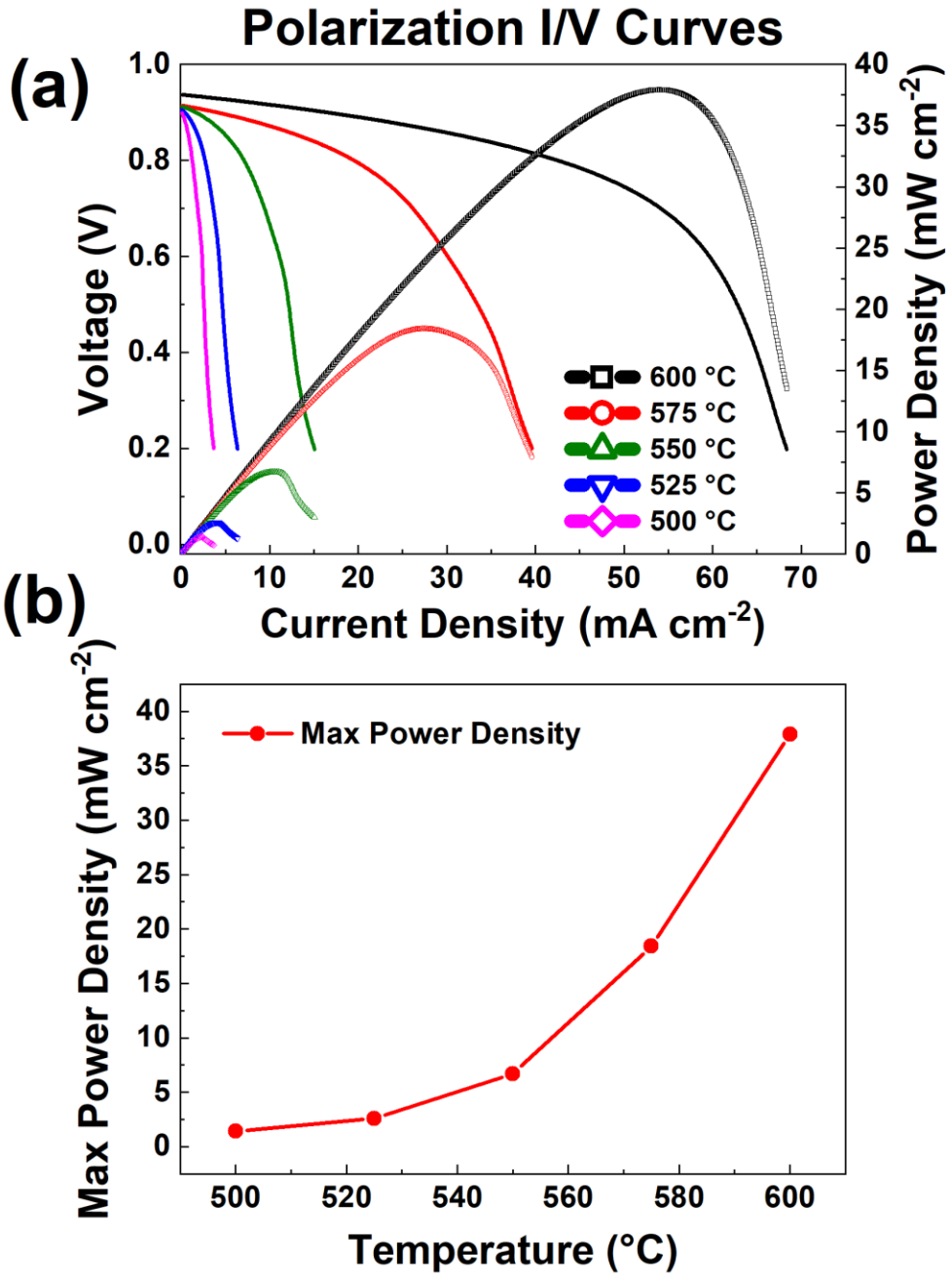

Figure 19 – Polarization curves measured on between 500-600 °C on a T9 NBFO/CGO/T9 NBFO symmetrical cell feeding air and 5% H_2 in Ar (a) Maximum power densities as a function of temperature (b).

are smaller than the theoretical Nernst potential, but this is expected for pure CGO electrolytes because of electron holes generation due to Ce^{4+} reduction in hydrogen at high temperatures [69]. The decrease in OCV is due to partial current leakage through the electrolyte associated with the electronic conductivity of CGO. The polarization curves were collected at a maximum of 600 °C to limit the ceria reduction and thus to maintain elevated the CGO ionic transference number and

the OCV. In addition, the measurements were performed in mild reducing conditions, such as wet 5% H_2 in Ar atmosphere, compared to dry pure H_2. The typical solution to avoid this OCV reduction is to deposit a thin electronic insulator YSZ layer on the fuel side of the CGO electrolyte [70]. Although the electrolyte support was not optimized, the symmetrical cell configuration was employed to demonstrate the feasibility of applying NBFO as both air and hydrogen electrodes simultaneously.

The maximum power densities are 1.4, 2.6, 6.6, 18.4, and 37.9 mW cm^{-2} at 500, 525, 550, 575 and 600 °C respectively. As expected, power density increases with the temperature. The maximum power density at 600 °C is comparable to the 40 mW cm^{-2} obtained for symmetrical cells based on cobalt-free $SrFe_{0.8}W_{0.2}O_{3-\delta}$ electrodes on CSO electrolyte measured at 600 °C in air and wet H_2 [22]. The performance can be further improved by optimizing the electrolyte-supported cell setup and boosting the conductivity using composite or infiltrated electrode configurations. However, the applicability of NBFO as electrodes for symmetrical SOFCs was successfully demonstrated.

4. Conclusion

This study focuses on investigating the suitability of perovskite ferrites, namely $PrBa_2Fe_3O_{8+\delta}$ (PBFO), $NdBa_2Fe_3O_{8+\delta}$ (NBFO), and $SmBa_2Fe_3O_{8+\delta}$ (SBFO) as electrodes for symmetrical SOFCs. The intrinsic properties of the synthesized compositions were measured under oxidizing and reducing conditions, followed by their performance as electrode materials using EIS. XRD confirms a cubic structure with the $Pm\bar{3}m$ symmetry for all samples. XRD under reducing and oxidizing environments demonstrates the stability of the materials without phase degradation. TEM investigation reveals the presence of quintuple perovskite nano-ordering only in SBFO samples, with an atomic plane arrangement of "Sm - Ba - Sm/Ba - Sm/Ba - Ba" along the *c*-axis direction. In SBFO, long-range variations in the quintuple structure orientation result in domains with different orientations within the same grain. Therefore, different domain orientations contribute to the cubic projection of the crystallographic structure observed by XRD. The quintuple nano-ordering is not clearly observed in NBFO and PBFO, indicating either the existence of tiny domains for the quintuple phase or the stabilization of a disordered cubic perovskite structure.

Dilatometry and *in situ* XRD measurements show that the samples exhibit a thermal expansion coefficient close to 14×10^{-6} K^{-1} at low temperatures, increasing to 30×10^{-6} K^{-1} above 600 °C.

This increment is related to the loss of oxygen with increasing temperature measured by TGA. PBFO exhibits the highest weight loss and thermal expansion coefficient among the samples, followed by NBFO and SBFO. The maximum electrical conductivity in air between 400-500 °C is 68, 43, and 9.3 S cm^{-1} for PBFO, NBFO, and SBFO, respectively. A significantly lower conductivity is observed in 5% H_2 in Ar due to oxygen loss and reduced charge carrier concentration across all samples.

The ASR of PBFO, NBFO, and SBFO electrodes are 0.26, 0.22, and 1.29 Ω cm^2 in air at 800 °C. The highest resistances are observed for SBFO, while NBFO and PBFO demonstrated promising performance. The disordered A-site structure is more efficient in the oxygen ion diffusion than the quintuple nano-ordered one observed for SBFO, as shown with MD simulations [43]. Additional improvements were achieved by reducing the synthesis temperature of NBFO powders down to 900 °C (T9 NBFO), reaching ASR values of 0.05 Ω cm^2 in air at 800 °C. Symmetrical fuel cell measurements were performed using T9 NBFO electrodes with improved microstructure in wet 5% H_2 in Ar and air between 500-600 °C. The I/V polarization curves reached peak power densities of 37.9, 6.7, and 1.4 mW cm^{-2} at 600, 550, and 500 °C respectively.

In conclusion, PBFO, NBFO, and SBFO show chemical and structural stability as symmetrical SOFC electrodes but are limited by the tiny electrical conductivity in reducing environments, as well as the significant thermal expansion coefficient in air. Fuel cell measurements on NBFO symmetrical cells indicate modest performance but demonstrate the applicability as symmetrical SOFC electrodes.

5. References

[1] Majerus S, Lauinger D, Van herle J. Cost Requirements for a Small-Scale SOFC Fed From Agricultural-Derived Biogas. Journal of Electrochemical Energy Conversion and Storage 2017;14. https://doi.org/10.1115/1.4035891.

[2] Marocco P, Gandiglio M, Santarelli M. When SOFC-based cogeneration systems become convenient? A cost-optimal analysis. Energy Reports 2022;8:8709–21. https://doi.org/10.1016/j.egyr.2022.06.015.

[3] Califano M, Sorrentino M, Rosen MA, Pianese C. Optimal heat and power management of a reversible solid oxide cell based microgrid for effective technoeconomic hydrogen consumption and storage. Applied Energy 2022;319:119268. https://doi.org/10.1016/j.apenergy.2022.119268.

[4] Md Harashid MA, Chen RS, Ahmad SH, Ismail AF, Baharuddin NA. Recent advances in electrode material for symmetrical solid oxide fuel cells and way forward sustainability based on local mineral resources. International Journal of Energy Research 2022;46:22188–221. https://doi.org/10.1002/er.8579.

[5] Zamudio-García J, Caizán-Juanarena L, Porras-Vázquez JM, Losilla ER, Marrero-López D. A review on recent advances and trends in symmetrical electrodes for solid oxide cells. Journal of Power Sources 2022;520:230852. https://doi.org/10.1016/j.jpowsour.2021.230852.

[6] Zhu K, Luo B, Liu Z, Wen X. Recent advances and prospects of symmetrical solid oxide fuel cells. Ceramics International 2022;48:8972–86. https://doi.org/10.1016/j.ceramint.2022.01.258.

[7] Østergård MJL, Mogensen M. *ac* Impedance study of the oxygen reduction mechanism on La1−xSrxMnO3 in solid oxide fuel cells. Electrochimica Acta 1993;38:2015–20. https://doi.org/10.1016/0013-4686(93)80334-V.

[8] Hansen KK, Wandel M, Liu Y-L, Mogensen M. Effect of impregnation of La0.85Sr0.15MnO3/yttria stabilized zirconia solid oxide fuel cell cathodes with La0.85Sr0.15MnO3 or Al2O3 nano-particles. Electrochimica Acta 2010;55:4606–9. https://doi.org/10.1016/j.electacta.2010.03.017.

[9] Ruiz-Morales JC, Marrero-López D, Canales-Vázquez J, Irvine JTS. Symmetric and reversible solid oxide fuel cells. RSC Adv 2011;1:1403–14. https://doi.org/10.1039/C1RA00284H.

[10] Sandoval MV, Cárdenas C, Capoen E, Pirovano C, Roussel P, Gauthier GH. Performance of La0.5Sr1.5MnO4±δ Ruddlesden-Popper manganite as electrode material for symmetrical solid oxide fuel cells. Part A. The oxygen reduction reaction. Electrochimica Acta 2019;304:415–27. https://doi.org/10.1016/j.electacta.2019.03.037.

[11] Sandoval MV, Cardenas C, Capoen E, Roussel P, Pirovano C, Gauthier GH. Performance of La0.5Sr1.5MnO4±δ Ruddlesden-Popper manganite as electrode material for symmetrical solid oxide fuel cells. Part B. the hydrogen oxidation reaction. Electrochimica Acta 2020;353:136494. https://doi.org/10.1016/j.electacta.2020.136494.

[12] Hjalmarsson P, Søgaard M, Mogensen M. Electrochemical performance and degradation of (La0.6Sr0.4)0.99CoO3 − δ as porous SOFC-cathode. Solid State Ionics 2008;179:1422–6. https://doi.org/10.1016/j.ssi.2007.11.010.

[13] Pelosato R, Cordaro G, Stucchi D, Cristiani C, Dotelli G. Cobalt based layered perovskites as cathode material for intermediate temperature Solid Oxide Fuel Cells: A brief review. Journal of Power Sources 2015;298:46–67. https://doi.org/10.1016/j.jpowsour.2015.08.034.
[14] Bucher E, Gspan C, Sitte W. Degradation and regeneration of the SOFC cathode material La0.6Sr0.4CoO3 − δ in SO2-containing atmospheres. Solid State Ionics 2015;272:112–20. https://doi.org/10.1016/j.ssi.2015.01.009.
[15] Choi HJ, Bae K, Jang DY, Kim JW, Shim JH. Performance Degradation of Lanthanum Strontium Cobaltite after Surface Modification. J Electrochem Soc 2015;162:F622. https://doi.org/10.1149/2.0971506jes.
[16] Simner SP, Bonnett JF, Canfield NL, Meinhardt KD, Shelton JP, Sprenkle VL, et al. Development of lanthanum ferrite SOFC cathodes. Journal of Power Sources 2003;113:1–10. https://doi.org/10.1016/S0378-7753(02)00455-X.
[17] Zurlo F, Di Bartolomeo E, D'Epifanio A, Felice V, Natali Sora I, Tortora L, et al. La0.8Sr0.2Fe0.8Cu0.2O3−δ as "cobalt-free" cathode for La0.8Sr0.2Ga0.8Mg0.2O3−δ electrolyte. Journal of Power Sources 2014;271:187–94. https://doi.org/10.1016/j.jpowsour.2014.07.183.
[18] Baharuddin NA, Muchtar A, Somalu MR. Short review on cobalt-free cathodes for solid oxide fuel cells. International Journal of Hydrogen Energy 2017;42:9149–55. https://doi.org/10.1016/j.ijhydene.2016.04.097.
[19] Hashim SS, Liang F, Zhou W, Sunarso J. Cobalt-Free Perovskite Cathodes for Solid Oxide Fuel Cells. ChemElectroChem 2019;6:3549–69. https://doi.org/10.1002/celc.201900391.
[20] Chen M, Paulson S, Thangadurai V, Birss V. Sr-rich chromium ferrites as symmetrical solid oxide fuel cell electrodes. Journal of Power Sources 2013;236:68–79. https://doi.org/10.1016/j.jpowsour.2013.02.024.
[21] Kong X, Zhou X, Tian Y, Wu X, Zhang J, Zuo W. Niobium doped lanthanum calcium ferrite perovskite as a novel electrode material for symmetrical solid oxide fuel cells. Journal of Power Sources 2016;326:35–42. https://doi.org/10.1016/j.jpowsour.2016.06.111.
[22] Su T, Li Y, Yang Y, Xu Z, Shi N, Wan Y, et al. Effect of tungsten doping on strontium ferrite electrode for symmetrical solid oxide electrochemical cell. International Journal of Hydrogen Energy 2020;45:23401–10. https://doi.org/10.1016/j.ijhydene.2020.06.111.
[23] Zheng K, Lach J, Czaja P, Gogacz M, Czach P, Brzoza-Kos A, et al. Designing high-performance quasi-symmetrical solid oxide cells with a facile chemical modification strategy for Sr2Fe2−xWxO6−δ ferrites electrodes with *in situ* exsolution of nanoparticles. Journal of Power Sources 2023;587:233707. https://doi.org/10.1016/j.jpowsour.2023.233707.
[24] Qiu P, Sun S, Li J, Jia L. A review on the application of Sr2Fe1.5Mo0.5O6-based oxides in solid oxide electrochemical cells. Separation and Purification Technology 2022;298:121581. https://doi.org/10.1016/j.seppur.2022.121581.
[25] Ma L, Wang Y, Li W, Guan B, Qi H, Tian H, et al. Redox-stable symmetrical solid oxide fuel cells with exceptionally high performance enabled by electrode/electrolyte diffuse interface. Journal of Power Sources 2021;488:229458. https://doi.org/10.1016/j.jpowsour.2021.229458.
[26] Taskin AA, Lavrov AN, Ando Y. Achieving fast oxygen diffusion in perovskites by cation ordering. Applied Physics Letters 2005;86:091910. https://doi.org/10.1063/1.1864244.
[27] Taskin AA, Lavrov AN, Ando Y. Fast oxygen diffusion in A-site ordered perovskites. Progress in Solid State Chemistry 2007;35:481–90. https://doi.org/10.1016/j.progsolidstchem.2007.01.014.

[28] Kim G, Wang S, Jacobson AJ, Reimus L, Brodersen P, Mims CA. Rapid oxygen ion diffusion and surface exchange kinetics in PrBaCo2O5+x with a perovskite related structure and ordered A cations. J Mater Chem 2007;17:2500–5. https://doi.org/10.1039/B618345J.
[29] Tarancón A, Burriel M, Santiso J, Skinner SJ, Kilner JA. Advances in layered oxide cathodes for intermediate temperature solid oxide fuel cells. J Mater Chem 2010;20:3799–813. https://doi.org/10.1039/B922430K.
[30] Parfitt D, Chroneos A, Tarancón A, Kilner JA. Oxygen ion diffusion in cation ordered/disordered GdBaCo2O5+δ. J Mater Chem 2011;21:2183–6. https://doi.org/10.1039/C0JM02924F.
[31] Lü S, Zhu Y, Fu X, Huang R, Guo Y, Zhang W, et al. A-site deficient Fe-based double perovskite oxides PrxBaFe2O5+δ as cathodes for solid oxide fuel cells. Journal of Alloys and Compounds 2022;911:165002. https://doi.org/10.1016/j.jallcom.2022.165002.
[32] Karen P, Woodward PM. Synthesis and structural investigations of the double perovskites REBaFe2O5+w (RE=Nd, Sm). J Mater Chem 1999;9:789–97. https://doi.org/10.1039/A809302D.
[33] Karen P. Oxygen nonstoichiometry in LnBaFe2O5+w across Ln = Nd, Sm, Gd. Journal of Solid State Chemistry 2021;301:122297. https://doi.org/10.1016/j.jssc.2021.122297.
[34] García-González E, Parras M, González-Calbet JM, Vallet-Regí M. A New "123" Family: *Ln*Ba2Fe3Oz: I. Ln = Dy, Ho. Journal of Solid State Chemistry 1993;104:232–8. https://doi.org/10.1006/jssc.1993.1158.
[35] García-González E, Parras M, González-Calbet JM, Vallet-Regí M. A New "123" Family: *Ln*Ba2Fe3Oz, (II), *Ln* = Nd, Sm, and Eu. Journal of Solid State Chemistry 1993;105:363–70. https://doi.org/10.1006/jssc.1993.1226.
[36] Karen P, Kjekshus A, Huang Q, Lynn JW, Rosov N, Natali Sora I, et al. Neutron and X-Ray Powder Diffraction Study of *R*Ba2Fe3O8+w Phases. Journal of Solid State Chemistry 1998;136:21–33. https://doi.org/10.1006/jssc.1997.7636.
[37] Lindén J, Karen P, Kjekshus A, Miettinen J, Karppinen M. Partial Oxygen Ordering in Cubic Perovskite *RE*Ba2Fe3O8+w (*RE*=Gd, Eu, Sm, Nd). Journal of Solid State Chemistry 1999;144:398–404. https://doi.org/10.1006/jssc.1999.8178.
[38] Karen P, Kjekshus A, Huang Q, Karen VL, Lynn JW, Rosov N, et al. Neutron powder diffraction study of nuclear and magnetic structures of oxidized and reduced YBa2Fe3O8+w. Journal of Solid State Chemistry 2003;174:87–95. https://doi.org/10.1016/S0022-4596(03)00180-4.
[39] Volkova NE, Lebedev OI, Gavrilova LYa, Turner S, Gauquelin N, Seikh MdM, et al. Nanoscale Ordering in Oxygen Deficient Quintuple Perovskite Sm2-εBa3+εFe5O15-δ: Implication for Magnetism and Oxygen Stoichiometry. Chem Mater 2014;26:6303–10. https://doi.org/10.1021/cm503276p.
[40] Kundu AK, Lebedev OI, Volkova NE, Seikh MM, Caignaert V, Cherepanov VA, et al. Quintuple perovskites Ln2Ba3Fe5−xCoxO15−δ (Ln = Sm, Eu): nanoscale ordering and unconventional magnetism. J Mater Chem C 2015;3:5398–405. https://doi.org/10.1039/C5TC00494B.
[41] Kundu AK, Yu Mychinko M, Caignaert V, Lebedev OI, Volkova NE, Deryabina KM, et al. Coherent intergrowth of simple cubic and quintuple tetragonal perovskites in the system Nd2−εBa3+ε(Fe,Co)5O15−δ. Journal of Solid State Chemistry 2015;231:36–41. https://doi.org/10.1016/j.jssc.2015.07.050.

[42] Volkova NE, Mychinko MYu, Golovachev IB, Makarova AE, Bazueva MV, Zyaikin EI, et al. Structure and properties of layered perovskites Ba1-xLnxFe1-yCoyO3-δ (Ln = Pr, Sm, Gd). Journal of Alloys and Compounds 2019;784:1297–302. https://doi.org/10.1016/j.jallcom.2018.12.391.
[43] Moazzam M, Li C, Cordaro G, Dezanneau G. Effect of A-site cation ordering on oxygen diffusion in NdBa2Fe3O8 through molecular dynamics. Journal of Solid State Chemistry 2023;325:124148. https://doi.org/10.1016/j.jssc.2023.124148.
[44] Cordaro G, Flura A, Donazzi A, Pelosato R, Mauvy F, Cristiani C, et al. Electrochemical characterization of PrBa2−xSrxCu3O6+δ layered oxides as innovative and efficient oxygen electrode for IT-SOFCs. Solid State Ionics 2020;348:115286. https://doi.org/10.1016/j.ssi.2020.115286.
[45] Li K, Niemczyk A, Świerczek K, Stępień A, Naumovich Y, Dąbrowa J, et al. Co-free triple perovskite La1.5Ba1.5Cu3O7±δ as a promising air electrode material for solid oxide fuel cells. Journal of Power Sources 2022;532:231371. https://doi.org/10.1016/j.jpowsour.2022.231371.
[46] Macias MA, Sandoval MV, Martinez NG, Vázquez-Cuadriello S, Suescun L, Roussel P, et al. Synthesis and preliminary study of La4BaCu5O13 + δ and La6.4Sr1.6Cu8O20 ± δ ordered perovskites as SOFC/PCFC electrode materials. Solid State Ionics 2016;288:68–75. https://doi.org/10.1016/j.ssi.2016.02.010.
[47] Irujo-Labalde XM de, Muñoz-Gil D, Urones-Garrote E, Ávila-Brande D, García-Martín S. Complex modulation of the crystal structure of a layered perovskite. A promising solid-oxide-fuel-cell cathode. J Mater Chem A 2016;4:10241–7. https://doi.org/10.1039/C6TA03307E.
[48] Zhou Q, Chen L, Cheng Y, Xie Y. Cobalt-free quintuple perovskite Sm1.875Ba3.125Fe5O15−δ as a novel cathode for intermediate temperature solid oxide fuel cells. Ceramics International 2016;42:10469–71. https://doi.org/10.1016/j.ceramint.2016.03.174.
[49] Petříček V, Dušek M, Palatinus L. Crystallographic Computing System JANA2006: General features. Zeitschrift für Kristallographie - Crystalline Materials 2014;229:345–52. https://doi.org/10.1515/zkri-2014-1737.
[50] Fergus JW. Electrolytes for solid oxide fuel cells. Journal of Power Sources 2006;162:30–40. https://doi.org/10.1016/j.jpowsour.2006.06.062.
[51] Cordaro G. Preparation of ink for electrode deposition via paint brushing using oxide powder. ProtocolsIo 2021. https://doi.org/10.17504/protocols.io.btm3nk8n.
[52] Volkova NE, Khvostova LV, Gavrilova LYa, Cherepanov VA. Role of Sm content to the crystal structure and properties of Sr1-xSmxFeO3-δ. Journal of Solid State Chemistry 2018;267:113–8. https://doi.org/10.1016/j.jssc.2018.08.007.
[53] Tietz F. Thermal expansion of SOFC materials. Ionics 1999;5:129–39. https://doi.org/10.1007/BF02375916.
[54] Dong F, Chen Y, Ran R, Chen D, Tadé MO, Liu S, et al. BaNb0.05Fe0.95O3−δ as a new oxygen reduction electrocatalyst for intermediate temperature solid oxide fuel cells. J Mater Chem A 2013;1:9781–91. https://doi.org/10.1039/C3TA11447C.
[55] Lu Y, Zhao H, Chang X, Du X, Li K, Ma Y, et al. Novel cobalt-free BaFe1−xGdxO3−δ perovskite membranes for oxygen separation. J Mater Chem A 2016;4:10454–66. https://doi.org/10.1039/C6TA01749E.

[56] Song X, Le S, Zhu X, Qin L, Luo Y, Li Y, et al. High performance BaFe1−xBixO3−δ as cobalt-free cathodes for intermediate temperature solid oxide fuel cells. International Journal of Hydrogen Energy 2017;42:15808–17. https://doi.org/10.1016/j.ijhydene.2017.05.061.
[57] Shannon RD. Revised effective ionic radii and systematic studies of interatomic distances in halides and chalcogenides. Acta Cryst A 1976;32:751–67. https://doi.org/10.1107/S0567739476001551.
[58] Tai L-W, Nasrallah MM, Anderson HU, Sparlin DM, Sehlin SR. Structure and electrical properties of La1 − xSrxCo1 − yFeyO3. Part 2. The system La1 − xSrxCo0.2Fe0.8O3. Solid State Ionics 1995;76:273–83. https://doi.org/10.1016/0167-2738(94)00245-N.
[59] Kulkarni A, Ciacchi FT, Giddey S, Munnings C, Badwal SPS, Kimpton JA, et al. Mixed ionic electronic conducting perovskite anode for direct carbon fuel cells. International Journal of Hydrogen Energy 2012;37:19092–102. https://doi.org/10.1016/j.ijhydene.2012.09.141.
[60] Steele BCH. Materials for IT-SOFC stacks: 35 years R&D: the inevitability of gradualness? Solid State Ionics 2000;134:3–20. https://doi.org/10.1016/S0167-2738(00)00709-8.
[61] Karen P, Kjekshus A. YBa2Fe3O8 with Varied Oxygen Content. Journal of Solid State Chemistry 1994;112:73–7. https://doi.org/10.1006/jssc.1994.1267.
[62] Öksüzömer MAF, Dönmez G, Sariboğa V, Altinçekiç TG. Microstructure and ionic conductivity properties of gadolinia doped ceria (GdxCe1−xO2−x/2) electrolytes for intermediate temperature SOFCs prepared by the polyol method. Ceramics International 2013;39:7305–15. https://doi.org/10.1016/j.ceramint.2013.02.069.
[63] Nielsen J, Hjelm J. Impedance of SOFC electrodes: A review and a comprehensive case study on the impedance of LSM:YSZ cathodes. Electrochimica Acta 2014;115:31–45. https://doi.org/10.1016/j.electacta.2013.10.053.
[64] Donazzi A, Cordaro G, Baricci A, Ding Z-B, Maestri M. A detailed kinetic model for the reduction of oxygen on LSCF-GDC composite cathodes. Electrochimica Acta 2020;335:135620. https://doi.org/10.1016/j.electacta.2020.135620.
[65] Mesguich D, Bassat J-M, Aymonier C, Brüll A, Dessemond L, Djurado E. Influence of crystallinity and particle size on the electrochemical properties of spray pyrolyzed Nd2NiO4+δ powders. Electrochimica Acta 2013;87:330–5. https://doi.org/10.1016/j.electacta.2012.07.134.
[66] Wu C, Wang Y, Hou Y, Li X, Peng Z, Du Q, et al. Reconstruction and optimization of LSCF cathode microstructure based on Kinetic Monte Carlo method and Lattice Boltzmann method. Chemical Engineering Journal 2022;436:132144. https://doi.org/10.1016/j.cej.2021.132144.
[67] Khandale AP, Kumar RV, Bhoga SS. Effect of synthesis route on electrochemical performance of PrBaCo2O5+δ cathode for IT-SOFC application. Bull Mater Sci 2023;46:119. https://doi.org/10.1007/s12034-023-02949-9.
[68] Steele BCH. Survey of materials selection for ceramic fuel cells II. Cathodes and anodes. Solid State Ionics 1996;86–88:1223–34. https://doi.org/10.1016/0167-2738(96)00291-3.
[69] Chiodelli G, Malavasi L. Electrochemical open circuit voltage (OCV) characterization of SOFC materials. Ionics 2013;19:1135–44. https://doi.org/10.1007/s11581-013-0843-z.
[70] Liu QL, Khor KA, Chan SH, Chen XJ. Anode-supported solid oxide fuel cell with yttria-stabilized zirconia/gadolinia-doped ceria bilayer electrolyte prepared by wet ceramic co-sintering process. Journal of Power Sources 2006;162:1036–42. https://doi.org/10.1016/j.jpowsour.2006.08.024.

Supplementary Material

Study of *RE*$Ba_2Fe_3O_{8+\delta}$ (*RE* = Pr, Nd, Sm) layered perovskites as cobalt-free electrodes for symmetrical solid oxide fuel cells

Milad Moazzam[a], Giulio Cordaro[a]*, Maxime Vallet[a], Vincent Boëmare[a], Nicolas Guiblin[a], Guilhem Dezanneau[a]

[a]Université Paris-Saclay, CentraleSupélec, CNRS, Laboratoire SPMS, 91190, Gif-sur-Yvette, France.

*Corresponding author: giulio.cordaro@centralesupelec.fr

Authors email: milad.moazzam@centralesupelec.fr – maxime.vallet@centralesupelec.fr – vincent.boemare@centralesupelec.fr – nicolas.guiblin@centralesupelec.fr – guilhem.dezanneau@centralesupelec.fr

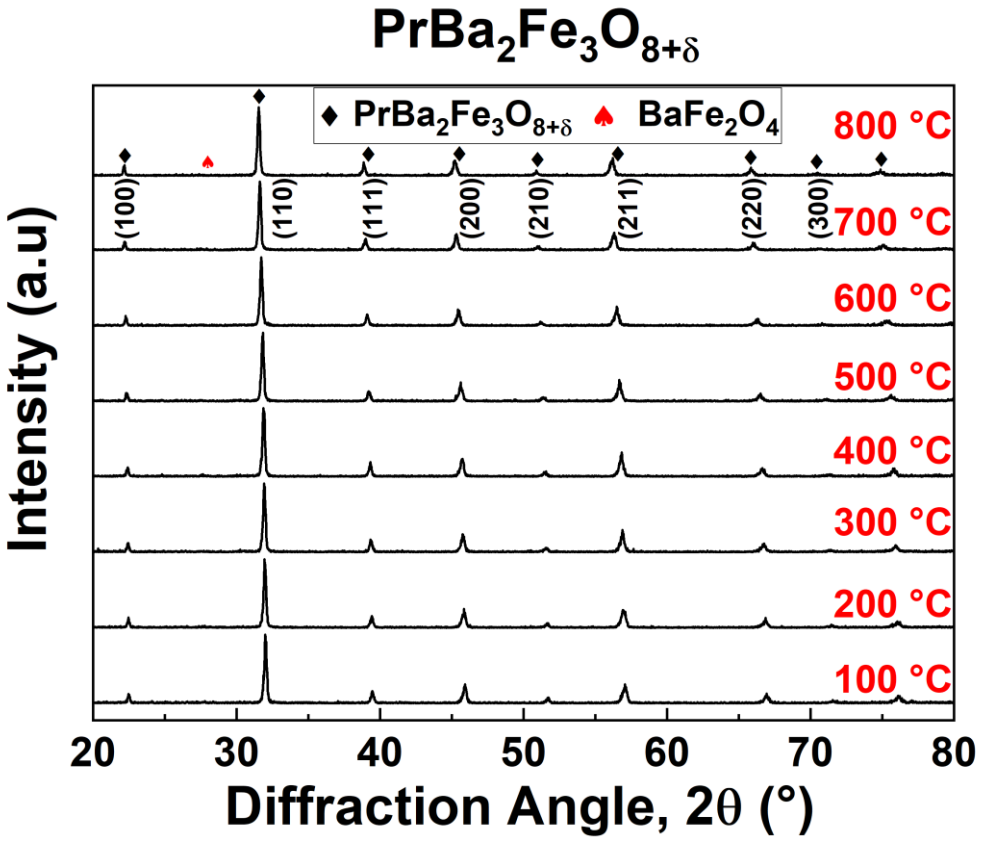

Figure S1 – High-temperature XRD diagrams of PBFO powder sample collected between 100 °C and 800 °C in air. Reflections related to the reference $PrBa_2Fe_3O_{8+\delta}$ phase ($Pm\bar{3}m$ symmetry, space group n° 221, ICSD n° 50898) are marked as black diamonds. The red spade symbol indicates the peak related to the $BaFe_2O_4$ impurity phase (PDF# 25-1191).

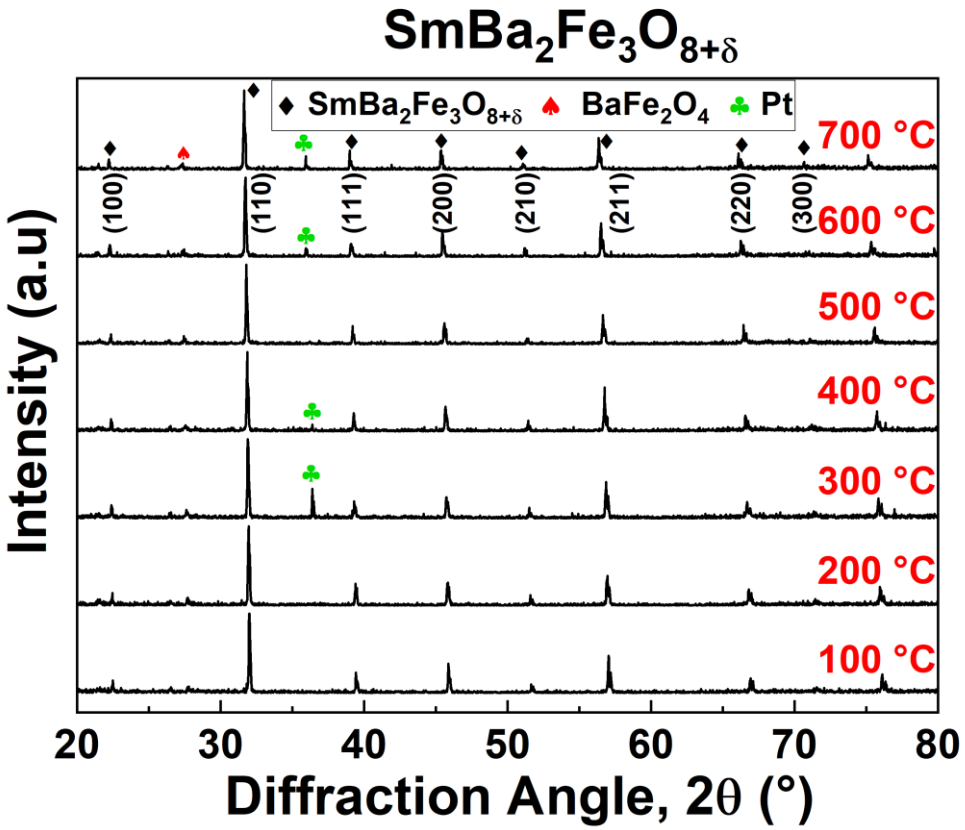

Figure S2 – High-temperature XRD diagrams of SBFO powder sample collected between 100 °C and 700 °C in air. Reflections related to the reference $SmBa_2Fe_3O_{8+\delta}$ phase ($Pm\bar{3}m$ symmetry, space group n° 221, PDF# 50-1849) are marked as black diamonds. The red spade symbol indicates the peak related to the $BaFe_2O_4$ impurity phase (PDF# 25-1191), and green clovers indicate Pt peaks related to the sample holder.

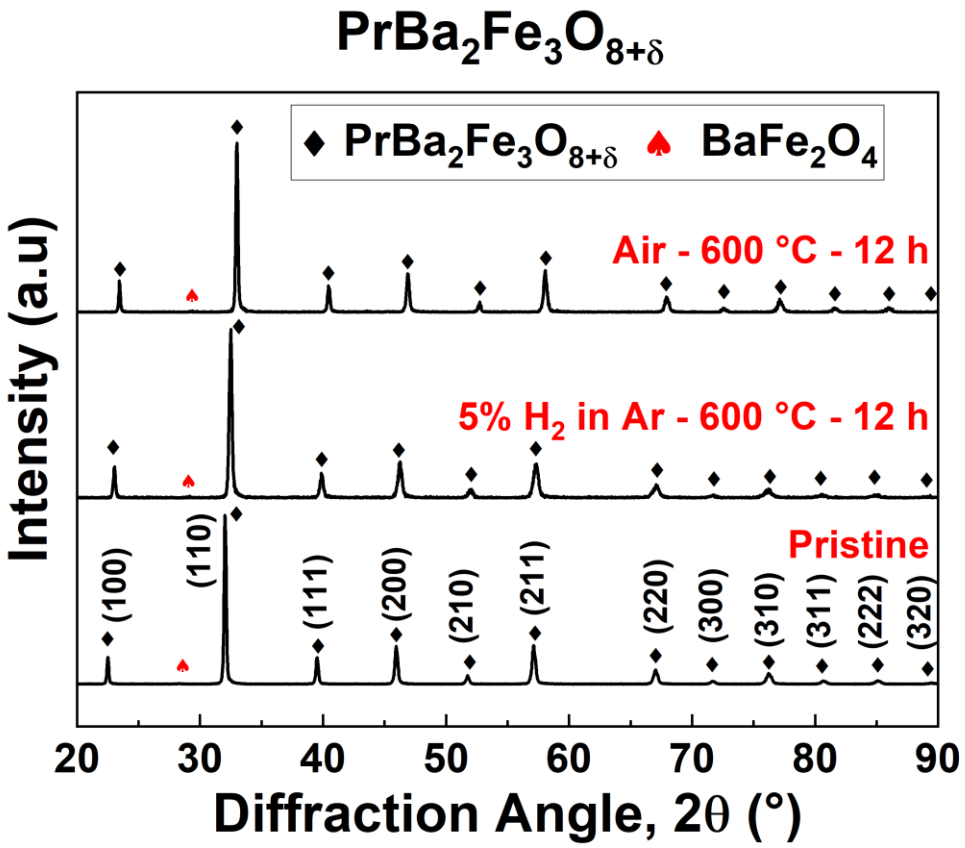

Figure S3 – XRD diagrams for PBFO after thermal treatment in oxidizing (Air) and reducing (5% H_2 in Ar) environments at 600 °C for 12 h. Reflections related to the reference $PrBa_2Fe_3O_{8+\delta}$ phase ($Pm\bar{3}m$ symmetry, space group n° 221, ICSD n° 50898) are marked as black diamonds. Red spade symbols indicate the peak related to the $BaFe_2O_4$ impurity phase (PDF# 25-1191).

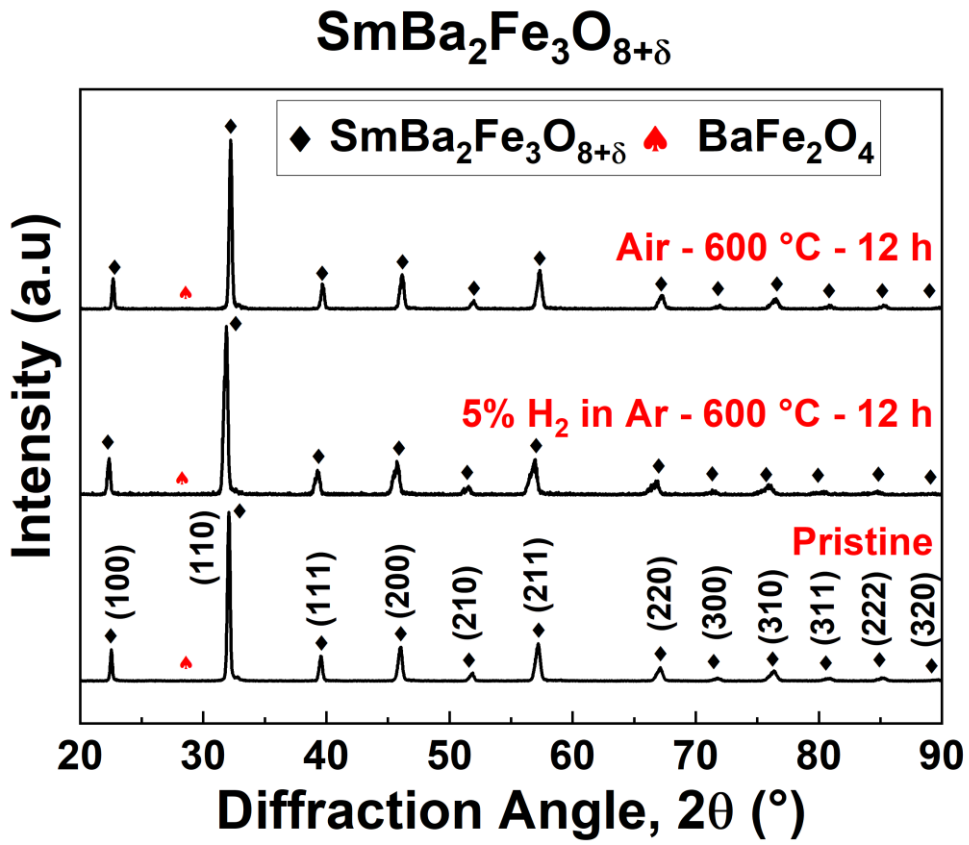

Figure S4 – XRD diagrams for SBFO after thermal treatment in oxidizing (Air) and reducing (5% H_2 in Ar) environments at 600 °C for 12 h. Reflections related to the reference $SmBa_2Fe_3O_{8+\delta}$ phase ($Pm\bar{3}m$ symmetry, space group n° 221, PDF# 50-1849) are marked as black diamonds. Red spade symbols indicate the peak related to the $BaFe_2O_4$ impurity phase (PDF# 25-1191).

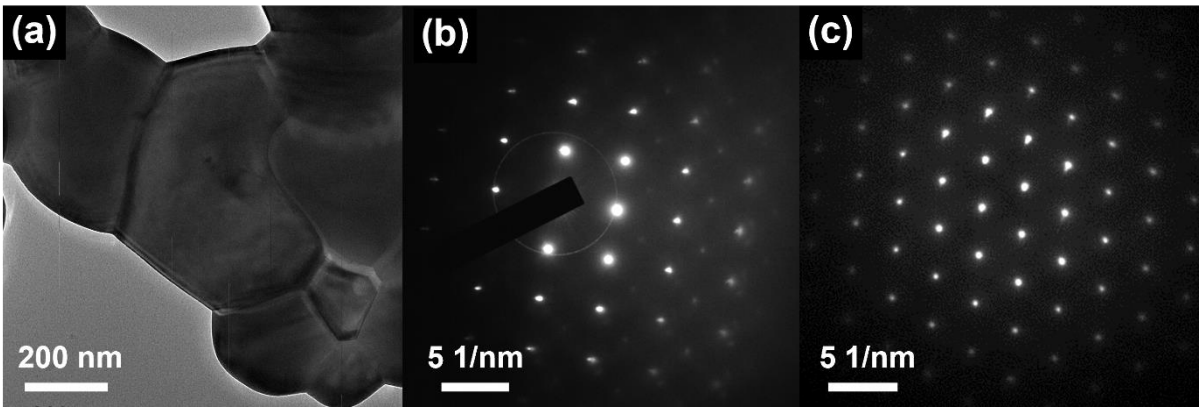

Figure S5 – Transmission electron microscopy (TEM) image of a polycrystalline PBFO nanoparticle (a) and selected area electron diffraction (SAED) images of different grains in the nanoparticle (b) and (c).

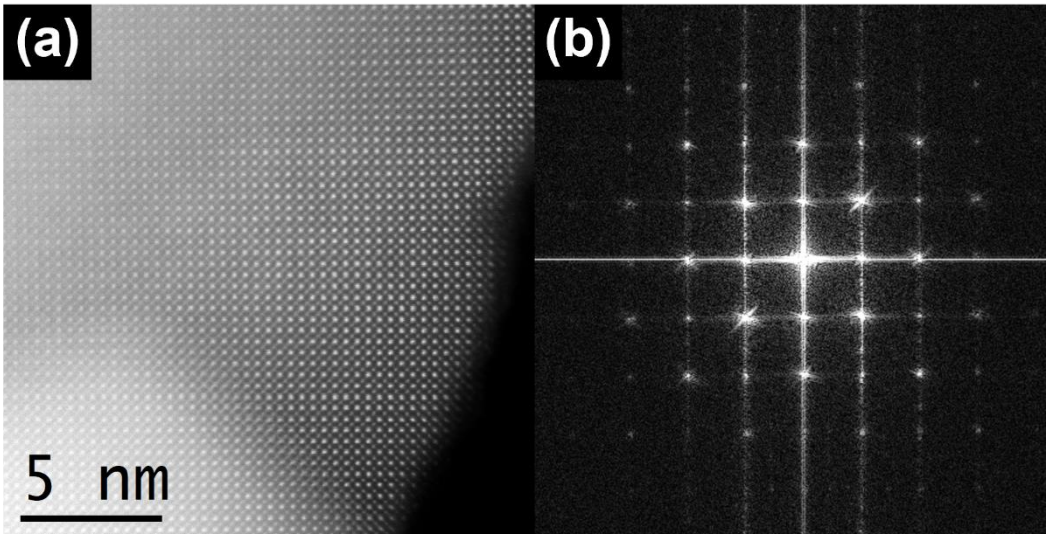

Figure S6 – High resolution high-angle annular dark-field scanning transmission electron microscopy (HAADF-STEM) image (a) and the corresponding fast Fourier transform (FFT) of a PBFO nanoparticle

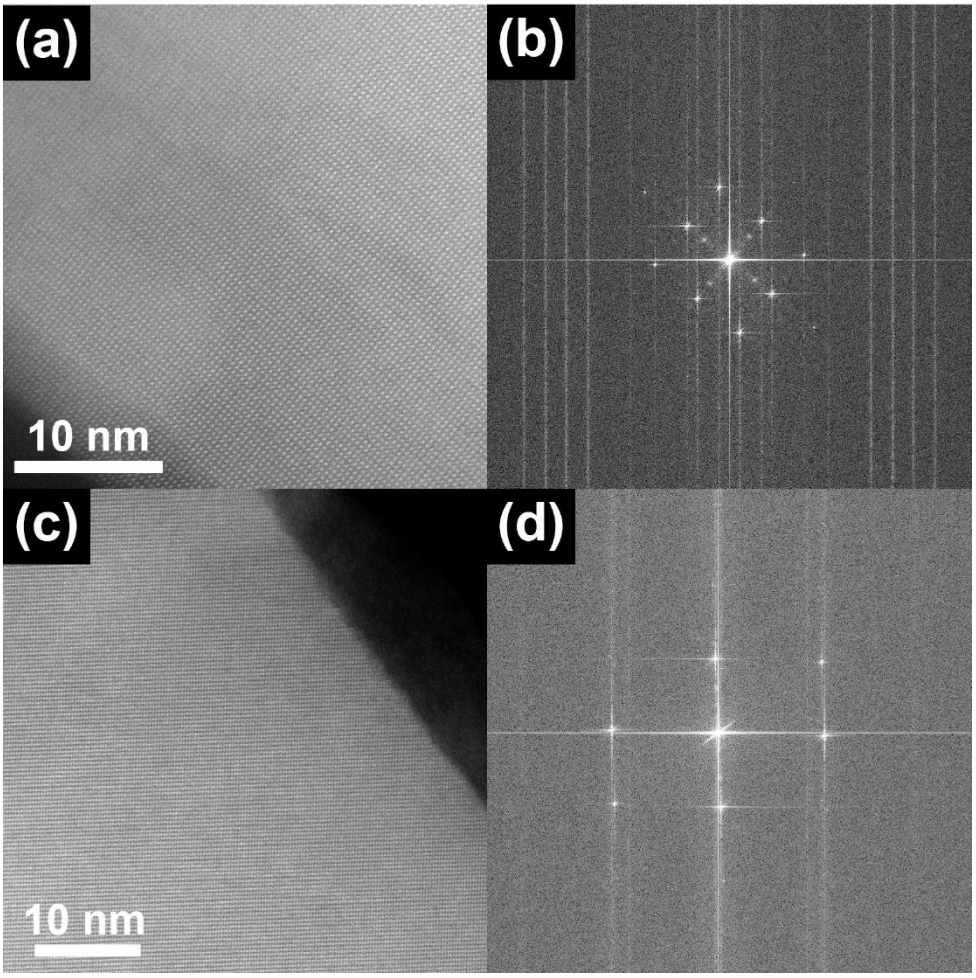

Figure S7 – High resolution HAADF-STEM images (a) and (c) of NBFO with the corresponding FFT images (b) qnd (d). Tiny domains of the nano-ordering superstructure are sparsely present (darker lines).